OCA-B/Pou2af1 Expression in T Cells Promotes PD-1 Blockade-Induced Autoimmunity but is Dispensable for Anti-Tumor Immunity

Junhong Du[1,2], Asit K. Manna[1,2], Miguel A. Medina-Serpas[3], Erik P. Hughes[1,2], Paulla Bisoma[1,2], Kimberley J. Evason[1,2], Arabella Young[1,2], W. David Wilson[4], Todd M. Brusko[3], Abdelbasset A. Farahat[5,6], Dean Tantin[1,2]

[1]University of Utah School of Medicine, Department of Pathology, Salt Lake City, UT, 84112, USA.

[2]University of Utah School of Medicine, Huntsman Cancer Institute, Salt Lake City, UT, 84112, USA.

[3] University of Florida College of Medicine, Department of Pathology, Immunology, and Laboratory Medicine, Diabetes Institute, Gainesville, FL 32610, USA.

[4]Georgia State University, Department of Chemistry, Atlanta, GA 30303, USA.

[5]California North State University, Master of Pharmaceutical Science Program, Elk Grove CA 95757, USA.

[6]Mansoura University, Department of Pharmaceutical Organic Chemistry, Faculty of Pharmacy, Mansoura 35516, Egypt.

Correspondence to Dean Tantin: dean.tantin@path.utah.edu

Short title: OCA-B Promotes PD-1 Blockade-Triggered Diabetes

Keywords OCA-B/Pou2af1; immune checkpoint inhibitors; autoimmune diabetes; Non-obese diabetic mouse; tumor immunity; MC38

Conflicts of interest statement: The authors have declared that no conflict of interest exists

Words in abstract: 237

Words main text: 6,634

Total main display items: 6

ABSTRACT

The transcription coregulator OCA-B promotes $CD4^+$ T cell memory recall responses and autoimmunity. OCA-B T cell deletion prevents spontaneous type-1 diabetes (T1D) onset in non-obese diabetic (NOD) mice and blunts T1D in a subset of more aggressive models. However, the role of OCA-B in diabetes induced by treatment with immune checkpoint inhibitors (ICIs), and the role of OCA-B in the control of tumors with and without ICI treatment, has not been studied. Here we show that islet and pancreatic lymph node T cells from T1D individuals express measurable *POU2AF1* mRNA. Deletion of OCA-B in T cells fully insulates 8-week-old non-obese diabetic (NOD) mice against ICI-induced diabetes and partially protects 12-week-old mice. Salivary and lacrimal gland infiltration and inflammation were also reduced. Protection was associated with a block in the differentiation of progenitor exhausted $CD8^+$ T cells (T_{PEX}) into terminally exhausted $CD8^+$ T cells (T_{EX}). We show that OCA-B T cell loss preserves anti-tumor immune responses following PD-1 blockade in different tumors and mouse strains. These findings point to a potential therapeutic window in which pharmaceuticals targeting OCA-B could be used to block the emergence of both spontaneous and ICI-induced autoimmunity while sparing anti-tumor immunity. We develop first-in-class small molecule inhibitors of Oct1/OCA-B transcription complexes and show that administration into NOD mice also blocks diabetes emergence following PD-1 blockade. These results identify OCA-B as a promising therapeutic target for the prevention of autoimmunity and immune-related adverse events (irAEs).

INTRODUCTION

Type 1 diabetes (T1D) affects 1.8 million people in the United States and incidence is increasing worldwide (*1-3*). It is characterized by autoimmune destruction of pancreatic β cells and consequent inability to produce insulin (*4*). While T1D symptoms can be managed with insulin injections, they must be taken for life. Transplantation of islets of Langerhans can restore insulin-independence to T1D patients, but results in reactivation of islet-specific memory cells T cells, β cell destruction and transplant rejection (*5, 6*). Similarly, engraftment of islets from non-obese diabetic (NOD) mice with severe combined immunodeficiency (NOD.SCID) into diabetic NODs briefly restores normoglycemia, but results in robust memory autoimmune responses and complete loss of grafted islet function in 10-14 days (*7*). Human therapies aim to minimize graft rejection or block the initial emergence of T1D in at-risk patients altogether while sparing normal immune function (*8*).

In humans, α-PD-1 therapy as well as therapies directed against a number of other inhibitory T cell receptors (immune checkpoint inhibitors or ICIs) are now used for treatment of a variety of cancer indications (*9-12*). The development and wide adoption of ICIs has resulted in a concomitant increase in associated unwanted immune-related adverse events, or irAEs, affecting a variety of tissues (e.g., skin, rheumatoid, pulmonary, gut, cardiac), some of which can be permanent (*10, 13-21*). IrAEs include endocrinopathies such as thyroiditis (*22*), and less frequently hypophysitis, autoimmune diabetes and other diseases (*17, 19, 21, 23*). A critical gap in the field is the identification of treatment strategies that block the emergence of irAEs while preserving anti-tumor immunity.

Polymorphisms in the *HLA-DR* and *HLA-DQ* genes encoding MHC class II have the strongest genetic influence on T1D, accounting for 40-50% of familial risk (*24*). These findings implicate $CD4^+$ T cells as primary drivers of pathogenesis. $CD4^+$ T cells direct other cell types such as $CD8^+$ T cells and macrophages to infiltrate pancreatic islets and cause β-cell destruction (*25*). Consistent with these findings, transient T cell depletion using α-CD3ε antibodies (Teplizumab-mzwv) significantly delays T1D onset in at-risk individuals in human clinical trials (*26-29*). Though promising, such treatments are limited by the resulting global immunosuppression. An ideal alternative would selectively deplete pathogenic T cell function while preserving beneficial immune function, including immunity against tumors.

OCA-B is a B cell- and T cell-restricted transcription coactivator (*30, 31*). In $CD4^+$ T cells, OCA-B docks with the transcription factor Oct1 (gene symbol *Pou2f1*) or Oct2/Pou2f2 to regulate targets including *Il2*, *Ifng*, *Icos*, *Csf2* and *Tbx21* (*32, 33*). Unlike transcription factors such as NFAT, AP-1 and NF-κB, OCA-B controls the expression of these genes specifically during repeated antigen exposures (*32, 33*). Agents targeting this pathway would selectively inhibit over-active T cell responses to antigen re-exposure but preserve acute immune response. Consistent with this prediction, in the absence of either OCA-B or Oct1 primary T cell responses to systemic and glial-tropic viruses (LCMV and JHMV, respectively) and viral clearance are normal (*31, 34*), however fewer central memory (T_{CM}) $CD4^+$ T cells form, and those that do are highly deficient in their ability to respond to antigenic re-challenge (*31, 33*). Three studies directly link polymorphisms in the human *OCAB* (*POU2AF1*) locus with autoimmune disease (*35-37*). Human polymorphisms affecting Oct1/2 (and therefore OCA-B) binding to the *TNFA* and *CTLA4* loci are associated with inflammatory bowel disease and systemic lupus erythematosus, respectively (*38, 39*). Additionally, two meta-analyses show a strong association between Oct1/Oct2/OCA-B binding site polymorphisms and autoimmunity including T1D(*40, 41*). Collectively, these studies link OCA-B with human autoimmunity.

92 OCA-B loss in T cells protects mice against spontaneous T1D onset (*42*). Single-cell RNA-sequencing
93 (scRNA-seq) reveals that protection is associated with loss of autoreactive $CD8^+$ T cell clones but
94 maintenance of the overall pancreatic islet immune architecture (*42*). These findings suggest that
95 targeting OCA-B could be used to treat T1D early in the disease course while sparing baseline
96 immunity. OCA-B's lymphoid-restricted expression pattern (*30, 31*), its dispensability for primary
97 antiviral responses (*31, 33, 34*), and its specificity for Oct1/Pou2f1 and Oct2/Pou2f2 complexes with
98 DNA (*43-45*) make it a promising therapeutic target that could be used to specifically block
99 autoreactive $CD4^+$ T cells while sparing normal immunity. OCA-B peptide mimics linked to membrane-
100 penetrating peptides can reduce inflammation and hyperglycemia in recent-onset T1D NOD mice, but
101 also show significant toxicity (*42*). An outstanding question is whether OCA-B can be successfully
102 targeted by more drug-like small molecules. It also remains to be determined if OCA-B promotes
103 diabetes driven by ICI therapy, and/or if OCA-B promotes anti-tumor immunity, including that
104 promoted by ICI.

105 Here, we identify T cells expressing POU2AF1 in the pancreatic lymph nodes and islets of T cells
106 expressing inflammatory markers in individuals with early T1D. We show that OCA-B in T cells
107 promotes the emergence of autoimmune diabetes following ICI administration in NOD mice, while
108 being dispensable for anti-tumor immune responses following ICI administration. We develop a small
109 molecule DNA-binding inhibitor that effectively disrupts Oct1:OCA-B complex in vitro and OCA-B's
110 transcription functions in cultured cells. We show that administration of these compounds to NOD
111 mice blocks the emergence of diabetes and prevents inflammation in pancreatic islets and other
112 endocrine organs following ICI administration, with in vivo efficacy tracking with activity in vitro.
113 Collectively, the findings indicate that OCA-B promotes diabetes development following ICI treatment,
114 and that targeting OCA-B could be used to block irAEs following ICI while sparing anti-tumor
115 immunity.

RESULTS

Detection of POU2AF1/OCAB mRNA in proinflammatory T cells in the setting of early human T1D

T cell conditional OCA-B loss protects NOD mice against spontaneous T1D (*42*). To identify a possible association with T cells in the context of human T1D, we performed a targeted reanalysis of previously published spatial transcriptomic data (*46*) using collated transcriptomic information from an individual with T1D (nPOD6551, 20 years old, 0.58 years duration) to identify $CD8^+$ T cells (pseudocolored yellow), B cells (green) and islet cells (white), as well as targeted transcript annotations for *CHGA* (pseudocolored red) to highlight β cells, *CD8A* (purple) to highlight T cells, *MS4A1* (orange) to highlight B cells. *POU2AF1* was pseudocolored cyan. Focusing on a representative islet with obvious insulitis, we observed strong peri-islet inflammation with both T cells and rare B cells (**Fig. 1A**). The B cells in the field all displayed obvious POU2AF1 gene expression as a positive control, while approximately 9.4% of $CD8^+$ T cells (19/202 cells) showed measurable *POU2AF1* expression. *POU2AF1*-expressing $CD4^+$ and $CD8^+$ T cells were also identified in the pancreatic lymph nodes (pLNs) from the same individual (**Fig. 1B-C**). These findings confirm the presence of *POU2AF1*-expressing T cells within the pancreas of T1D patients.

OCA-B T cell knockout protects NOD mice against diabetes induced by PD-1 blockade

Modulating the PD-1 pathway induces diabetes and other endocrinopathies in NOD mice (*47-50*). To test the effect of OCA-B T cell loss in diabetes induced by PD-1 blockade, we treated 8-week-old male NOD mice with four injections of α-PD-1 antibody to follow the disease timecourse, or one injection of α-PD-1 antibody with a 5-day interval prior to flow cytometric analysis of NOD mice (**Fig. 2A**). OCA-B loss in T cells completely blocked α-PD-1-induced diabetes development (**Fig. 2B-C**). Treatment of 12-week-old female NOD mice with 5 total injections of α-PD-1 resulted in less complete protection, with half the mice failing to develop diabetes and the other half showing delayed onset (**fig. S1A-B**). Flow cytometry revealed a significant reduction in islet-infiltrating $CD45^+$ leukocytes in α-PD-1-treated knockout mice compared to littermate controls (**Fig. 2D-E**). We also observed a decrease in the ratio of islet-infiltrating $CD8^+/CD4^+$ T cells in 8-week-old knockouts (**Fig. 2F-G**). Autoreactive $CD8^+$ T cells specifically recognize and destroy β cells and their relative numbers tend to increase with PD-1 blockade (*25*). Among the infiltrating $CD8^+$ cells, there were no changes in total $CD11a^+CD62L^{lo}$ activated cells (**Fig. 2H-I**), suggesting that OCA-B does not regulate acute activation in this context, however $CD8^+PD\text{-}1^+$ cells were significantly reduced (**Fig. 2J-K and fig. S1C-D**). PD-1 blockade results in the proliferation and differentiation of exhausted $CD8^+$ T cells in pancreatic islets, promoting the expansion of both T_{PEX} and T_{EX} cells but also skewing the islet total exhausted T cell population in favor of T_{EX} (*25*). To determine the effect of OCA-B loss on this pathogenic maturation, we used SLAMF6 (also known as Ly108) and CD39 to distinguish $CD8^+$ T_{PEX} and T_{EX}, respectively, at both 8 and 12 weeks. OCA-B loss resulted in a marked diminution in T_{EX} percentages among both $PD\text{-}1^+CD8^+$ and total islet cells (**Fig. 2L-M**), consistent with a defect in the ability of $CD8^+$ T_{PEX} cells within the islets of 8-week-old mice to differentiate into T_{EX}. Similar findings were made at 12 weeks though with decreased magnitude (**fig. S1E-F**). A similar decrease of $SLAMF6^-CD39^+$ terminally exhausted $CD4^+$ T cells was also observed (**fig. S1G-H**). In the absence of α-PD-1 treatment, T_{PEX} percentages

158 were unaffected while knockouts still showed a substantial decrease in T_{EX}, suggesting that the
159 differences in T_{EX} with α-PD-1 treatment are not due to prior differences in T_{PEX} abundance in the
160 knockouts (**fig. S2A-B**). Lastly, following PD-1 blockade in 8-week-old animals, we observed stark
161 differences in the accumulation of CD62L^{hi} T_{PEX}, an even more developmentally plastic CD8^{+}
162 subpopulation (*51*) (**fig. S2C-D**). Cumulatively, these results indicate that OCA-B loss in T cells blocks
163 the induction of diabetes by α-PD-1 treatment and reduces the pathogenic maturation of CD8^{+} T_{PEX} in
164 the pancreatic islets.

165

166 **OCA-B T cell knockout maintains anti-tumor immunity induced by PD-1 blockade**

167 To determine if OCA-B T cell loss has a corresponding effect on anti-tumor immunity, we used
168 C57BL/6 and NOD mice OCA-B conditional knockout mice (*31, 42*) with syngeneic tumor lines. In the
169 C57BL/6 strain background we used two lines, B16F10 and MC38. Compared to littermate controls
170 lacking the CD4-Cre driver, OCA-B loss had no effect on B16F10 tumor growth (**fig. S3**). This result
171 was expected because unmodified B16 cells do no elicit robust immune responses unless given a
172 combination of ICI treatment (*52*). In contrast, "immune-hot" MC38 colon adenocarcinoma cells exhibit
173 significant control by T cells that can be augmented by α-PD-1 treatment (*53*). We found that MC38
174 tumor control was preserved with OCA-B T cell loss either in the absence or presence of α-PD-1
175 treatment (**Fig. 3A-B**). Flow cytometry of cells from the tumor microenvironment (TME) showed
176 equivalent CD45.2^{+} leukocyte infiltration and CD8^{+} to CD4^{+} T cell ratios with α-PD-1 treatment (**Fig.**
177 **3C-D**). The percentages of CD4^{+} and CD8^{+} SLAMF6^{+}CD39^{-} and SLAMF6^{-}CD39^{+} cells in the TME
178 following α-PD-1 antibody treatment were similar between OCA-B knockouts and controls (**Fig. 3E-F**).
179 T cell exhaustion in tumor-infiltrating CD4^{+} and CD8^{+} as indicated by TIM-3 expression was also
180 equivalent (**Fig. 3G-H**).

181 Because the protection from PD-1 blockade-induced diabetes was observed using NOD background
182 mice, we also assessed tumor responses using a syngeneic "immune-hot" 9495 sarcoma cell line
183 (*54*), allowing us to measure diabetes incidence and tumor control in the same animals. α-PD-1
184 antibody treatment was effective in controlling 9495 tumor growth in syngeneic NOD mice (**Fig. 4A**)
185 as expected (*54*). Moreover, tumor control either with or without α-PD-1 treatment was equivalent
186 regardless of OCA-B status (**Fig. 4A**). A similar cohort of mice were again fully protected against
187 diabetes in the OCA-B deficient group, though penetrance in the control group was lower due to the
188 decreased amount of α-PD-1 antibody used (200 μg vs. 250 μg) to slow diabetic progression and
189 allow longer monitoring of tumor growth (**fig. S4A**). Although statistically nonsignificant, there was a
190 trending decrease in CD45^{+} leukocyte tumor infiltration in OCA-B-deficient mice (**Fig. 4B**). This was
191 driven by 4 control animals with high tumor infiltrate levels. As with MC38 tumors in C57BL/6 mice,
192 CD8^{+} percentages, T_{PEX} to T_{EX} differentiation, and CD8^{+} TIM-3 expression (**Fig. 4C-H**) were equivalent
193 in the context of α-PD-1 treatment. There were also few differences in CD4^{+} and CD8^{+} T cell activation
194 and PD-1 expression (**fig. S4B-E**). These findings indicate minimal differences in anti-tumor immune
195 responses to multiple syngeneic tumor lines in OCA-B T cell knockout mice, indicating a divergence
196 between anti-tumor immunity and the precipitation of irAEs that could be leveraged therapeutically.

197

198 **Development of small molecule inhibitors of Oct1:OCA-B complexes**

199 The Oct1:OCA-B:DNA co-crystal structure (*45*) suggests multiple possible targeting strategies,
200 including rationally designed OCA-B peptide mimics (**Fig. 5A**, upper lightning bolt) which are
201 functional but associated with toxicity in cells and mice due to the membrane-penetrating peptide (*42*).
202 To identify novel small molecule inhibitors, we used another strategy in which DNA minor groove-
203 binding compounds with specificity for the consensus octamer motif (5'ATGCAAAT) would disrupt
204 Oct1:OCA-B complexes. These inhibitors would dock on the underside of the DNA in the structure
205 shown in **Fig. 5A** (bottom lightning bolt) and would interfere with the unstructured Oct1 linker domain
206 that also spans the minor groove. We synthesized and tested 9 candidate minor groove-binding
207 compounds with specificity for the octamer motif. To test efficacy, we developed two cell-based assay
208 systems. The first is a transcription-based platform in which we stably transfected the human T cell
209 line SupT1 to express secreted nanoluciferase (nLuc) under the control of five Oct1/OCA-B binding
210 sites. SupT1 T cells express OCA-B at higher levels than, e.g. Jurkat cells, and at levels comparable
211 to primary thymocytes (**Fig. 5B**). We generated a stable-transfected SupT1 clone expressing nLuc
212 under the control of five wild-type octamer sequences ("5×Oct") and a second using mutant sites
213 incapable of binding Oct1 and OCA-B ("5×Mut", **Fig. 5C**). The 5×Oct clone produced substantial levels
214 of luciferase activity relative to empty vector-transduced controls, while the 5×Mut clone expressed
215 lower but still measurable activity (**Fig. 5D**). Timecourse experiments show that 12- to 18-hr
216 incubations have not yet saturated nLuc activity and capture a dynamic range allowing both activators
217 and inhibitors to be detected (**Fig. 5E**). We therefore chose 18-20 hr for all further experiments. Cell
218 counts were also taken to measure cell viability, using 2.5 μM staurosporine a positive control for
219 maximum toxicity. The treatment kills >98% of SupT1 cells within ~20 hr and correspondingly inhibits
220 luciferase expression (**fig. S5**). Of the 9 candidate compounds two – DB1033 (IC_{50}~26 μM, **Fig. 5F**)
221 and DB2232 (IC_{50}~10 μM, **fig. S6A**) – inhibited luciferase activity without significantly affecting
222 luciferase expression from the mutant cell line and without significant toxicity. Other compounds such
223 as DB2658 showed significant toxicity in the same screen (**fig. S6B**) or were less active (e.g.,
224 DB2385, **fig. S6C-H**). The DB1033 structure is shown in **Fig. 5G**. Molecular docking indicated that
225 DB1033 preferentially interacts with DNA minor groove in the AAAT portion of the consensus octamer
226 sequence, overlapping with the location of the unstructured Oct1 linker domain (**Fig. 5H-I**).

227 To reduce the possibility of off-target hits, we tested DB1033 compound activity using an orthogonal
228 cell-based method. We developed a nano-bioluminescence resonance energy transfer (NanoBRET)
229 assay that measures OCA-B's interaction with its cognate transcription factor Oct1. In this assay,
230 293T cells are co-transfected with an OCA-B construct carrying a HaloTag and an Oct1 construct
231 carrying an nLuc tag (**Fig. 6A**). DB1033 again showed dose-dependent inhibition (**Fig. 6B**), indicating
232 that DB1033 disrupts the interaction between Oct1 and OCA-B. To test this prediction at a mechanism
233 level, we used electrophoretic mobility shift assays (EMSA) with recombinant Oct1 DNA binding
234 domain and recombinant full-length OCA-B to measure formation of Oct1:OCA-B:DNA complexes
235 (**Fig. 6C**). We used Cy5-conjugated double-stranded DNA to visualize complexes with cognate DNA
236 in native polyacrylamide gels. Labeled DNA was in excess relative to protein such that changes in the
237 ability to form a complex can be readily observed. Because of "caging effects", changes in off-rates
238 are not efficiently captured within a running native gel. Instead, in this assay effects of an inhibitor on
239 complex formation are likely generated during the incubation prior to gel loading. We assembled the
240 protein, DNA and buffer components on ice for 25 minutes in stringent conditions (150 mM KCl), and
241 incubated the mixture for a further 5 min at room temperature ±compound prior to loading. Oct1
242 readily formed a complex with DNA that was augmented and slightly supershifted in the presence of

243 OCA-B, indicating the formation of a ternary complex (**Fig. 6D**, lane 3). Inclusion of DB1033 efficiently
244 disrupted complex formation in a dose-dependent manner (lanes 4-7).

245 A complementary in vitro assay uses differential scanning fluorimetry (nanoDSF) to measure
246 Oct1:OCA-B:DNA complex thermal stability. NanoDSF measures the gradual exposure of UV-
247 absorbing tyrosine side chains as proteins unfold with increasing temperature. We developed a
248 single-polypeptide chimeric molecule containing the Oct1 DNA binding domain fused to the first 44
249 amino acids of OCA-B, encompassing the structured part of OCA-B that contacts Oct1 (**Fig. 6E**). The
250 first 15 amino acids of OCA-B do not appear to be well-structured and presumably serve as a linker
251 between the two molecules. AlphaFold 3 (*55*) predicts that the chimeric molecule folds similarly to
252 natural Oct1 and OCA-B on DNA (**Fig. 6F**). The protein was expressed in *E. coli* with N-terminal 6-
253 His, consecutive C-terminal Twinstrep and FLAG tags. Following purification, the protein was found to
254 be mostly pure as assessed by Coomassie staining SDS-PAGE (**fig. S7A**). Size exclusion
255 chromatography indicated that the purified protein was mostly monodisperse, and EMSA indicated
256 that it was able to interact with consensus octamer DNA (**fig. S7B-C**). The presence of target DNA
257 strongly increased the stability of the chimeric protein in nanoDSF, as expected (**Fig. 6G**), while
258 adding DB1033 in the presence of DNA destabilized the complex (**Fig. 6H**). These findings identify
259 DB1033 as the best compound tested, indicate that DB1033 acts to disrupt Oct1:OCA-B complexes
260 on DNA, and establish a pipeline for assessing molecules that modulate Oct1 and/or OCA-B's
261 interactions with one another and with DNA, their overall stability, and their transcriptional functionality.

262

263 **Small molecule Oct1:OCA-B inhibitors block α-PD-1-induced diabetes and other irAEs in NOD**
264 **mice**

265 We treated 8-week-old male NOD mice with five *i.p.* injections of 15 mg/kg DB1033 or DB2232
266 simultaneously with α-PD-1 antibody treatment, plus one additional dose of compound on day 11. 8-
267 week-old male NOD.*Ocab*$^{fl/fl}$;CD4-Cre mice were used as a positive control for protection. As with
268 genetic OCA-B T cell knockout, DB1033 treatment completely protected mice against diabetes
269 emergence (**Fig. 7A-B**). These results indicate 1) that DB1033 is effective in protecting mice against
270 α-PD-1 antibody-induced diabetes, and that 2) acute inhibition at the same time as α-PD-1 antibody
271 delivery is sufficient to protect mice against diabetes development. DB1033 toxicity was negligible or
272 low-level, as there was a trending but statistically nonsignificant loss of weight associated with treated
273 animals at endpoint (**Fig. 7C**). Protection was not only confined to the pancreatic islets but was also
274 noted with salivary and lacrimal gland tissues, where leukocyte infiltration was strongly reduced (**Fig.**
275 **7D-E**). Importantly, the structurally related DB2232 compound, which was inferior in cell-based
276 assays, was also functionally inferior at preventing diabetes (**fig. S7D-F**). These findings provide
277 evidence of a structure-activity relationship linking compound activity to OCA-B complex inhibition. In
278 summary, the findings show firstly that OCA-B promotes the development of irAEs in ICI-treated NOD
279 mice while being dispensable for anti-tumor immunity, and secondly that acute small molecule
280 inhibitor administration also blocks irAE generation.

DISCUSSION

Here we show that OCA-B expression in T cells promotes irAEs following ICI treatment while minimally affecting anti-tumor responses. We also, for the first time, show that a small molecule Oct1:OCA-B inhibitor phenocopies the protection against irAEs observed using the OCA-B T cell knockouts. The latter findings indicate that acute OCA-B inhibition is sufficient to protect against irAEs and suggest the existence of a therapeutic window in which OCA-B pharmacological targeting can be used to block autoimmunity while sparing baseline immune function, including immunity to tumors.

OCA-B is one of three tissue-restricted transcription coregulators known as OCA proteins: OCA-B, OCA-T1 and OCA-T2 (*56*). Like the other two proteins OCA-B docks with the sequence-specific DNA binding POU transcription factors to regulate transcription (*43-45*). The OCA-Ts are master regulators of tuft cells, and a therapeutic vulnerability in small cell lung cancers originating from this cell type (*56*). OCA-B has important B cell-intrinsic functions including in the formation of germinal centers (*57, 58*). In T cells, OCA-B docks with the POU factor Oct1 to regulate target genes encoding cytokines and other immunomodulatory proteins (*33*). Because OCA-B expression is 50-100-fold higher in B cells compared to T cells (*31*), a calibrated dose of competitive inhibitor could selectively block T cell functions while sparing B cell-intrinsic OCA-B functions. For all three proteins, whole-body null mice are healthy, viable and fertile (*56, 59, 60*), suggesting that they a good candidate drug targets, however no small molecules targeting OCA proteins have been described.

Multiple lines of evidence show that pathogenic human and mouse progenitor-like T cells promote and sustain autoimmunity including T1D (*51, 61-63*). In mice, OCA-B promotes pathogenesis in experimental autoimmune encephalomyelitis (EAE), a model of multiple sclerosis, through maturation of stem-like cells into encephalitogenic effectors (*34*). These properties are T cell intrinsic. In a relapsing-remitting NOD.EAE model, OCA-B T cell-deficiency specifically protects mice from relapse (*34*). On the NOD background, both OCA-B whole body and T cell-specific knockout block the onset of spontaneous T1D (*42*). Using more aggressive T1D mouse models including CD25-mediated T_{reg} depletion and the CD8-restricted, autoreactive NY8.3 transgenic line revealed partial protection, while using the CD4-restricted BDC2.5 and CD8-restricted RIP-mOVA-OT-1 models showed no differences (*42*). The protection conferred by OCA-B loss is therefore strongest in more chronic polyclonal models. These findings also reveal that OCA-B T cell loss does not result in global immunosuppression, which would result in broader protection. In female NOD mice with newly arisen T1D, intravenous administration of membrane-penetrating OCA-B peptide mimics briefly reverses elevated blood glucose, as well as pancreatic islet T cell infiltration and pro-inflammatory cytokine production (*42*). In contrast to the pancreas, pLN showed no change in T cell numbers or percentages, but did show reduced T cell cytokine responses following self-peptide stimulation (*42*). However, greater than three peptide injections was toxic, with mice exhibiting ruffled skin, moribund appearance and weight loss (*42*). The Tat membrane-penetrating peptide is associated with acute toxicity that can be mitigated by spacing the dose(*64-66*).

The ability to trigger endocrine irAEs using α-PD-1 treatment in NOD mice presented an opportunity to test the OCA-B T cell loss of function model in different ways. First, to test the effect of OCA-B loss in an aggressive but physiologically relevant model of autoimmune diabetes. Second, to use the diabetes and other pathologies as models for ICI-triggered irAEs. Third, to determine the role of OCA-B in anti-tumor immunity, given the importance of finding anti-irAE treatments that do not inhibit tumor control for patients with cancer. We found that OCA-B T cell loss protected NOD mice against ICI-triggered diabetes. The effect of OCA-B loss was partially dependent on the age at which ICI was

325 administered, with 8-week-old mice showing more complete protection compared to 12-week-old
326 mice. This finding is consistent with a model in which OCA-B loss protects NOD mice at multiple
327 levels, one of which spans the 8-week timepoint and is PD-1 independent, and one of which spans
328 the 12-week timepoint and is partially PD-1 dependent. Profiling the immune cells in these mice flow
329 cytometrically indicated significant reduction in T_{EX}, and a concomitant increase in cells with a
330 progenitor-like (SLAMF6^{hi}CD39^{lo}) phenotype.

331 In contrast to the autoimmune protection conferred by OCA-B loss, immune responses and tumor
332 control were preserved either with or without α-PD-1 treatment. No differences were observed using
333 immune-cold B16F10 melanoma cells, as well as immune-hot MC38 colon carcinoma cells and 9495
334 sarcoma cells. Similar to the preservation of tumor control, loss of OCA-B in T cells preserves normal
335 primary response and viral control following infection with either the acute strain of lymphocytic
336 choriomeningitis virus (LCMV) or the glial-tropic β-coronavirus JHMV (*31, 33, 34*). The normal T cell
337 primary immune response phenotypes observed with Oct1 and OCA-B genetic deletion suggest the
338 existence of a therapeutic window in which an OCA-B pharmaceutical could be used not just to block
339 autoimmunity, but could be co-administered with ICIs to block irAEs while sparing immunity to viruses
340 and tumors. A likely side effect of therapies targeting this pathway would be an inability of newly-
341 generated memory CD4$^+$ T cells to mount robust recall responses (*31, 33*). Our findings indicate that
342 OCA-B promotes a memory-like population of CD4$^+$ T cells important for immune responses to tumor
343 re-challenge and relapse (manuscript in prep). An OCA-B inhibitor may therefore need to be
344 withdrawn prior to any potential tumor relapse.

345 Despite the prevailing but erroneous idea that transcription factors are "undruggable," there are
346 multiple historical(*64, 67-69*), and recent(*70-84*) counterexamples, the latter enabled by technologies
347 such as PROTAC(*85, 86*). Oct1's wide expression pattern and role in somatic stem cell function (*87,*
348 *88*) make it less attractive as a drug target relative to OCA-B, which is highly tissue-specific. Whole-
349 body OCA-B knockouts are viable and fertile (*59, 60*). We show that systemic administration of a
350 small molecule inhibitor, DB1033, into NOD mice blocks the emergence of α-PD-1-induced diabetes.
351 These molecules disrupt Oct1:OCA-B:DNA complexes in cell culture and in vitro. The finding that
352 DB1033 administration concomitant with α-PD-1 antibody treatment is sufficient to block the induction
353 of diabetes and other autoimmune pathologies suggests that OCA-B actions close to the time of
354 injection, and therefore spatially proximate to the pLNs and pancreatic islets, rather than development
355 of auto-reactive T cells in an OCA-B deficient environment from the double-positive thymocyte stage
356 onwards, mediates autoimmune protection. Moreover, we show that a structurally related compound,
357 DB2232, that is inferior in attenuating OCA-B-dependent transcription in cell culture and in disrupting
358 Oct1:OCA-B complexes in vitro is also functionally inferior at protecting NOD mice against ICI-
359 triggered diabetes, strongly suggesting that these compounds act through OCA-B disruption. These
360 reagents provide a conceptual milestone as a first-in-class small molecule Oct1/OCA-B inhibitor that
361 can reduce autoimmunity. More work is necessary to develop superior and more drug-like small
362 molecule inhibitors.

MATERIALS AND METHODS

Design

The objective of the study was to determine the effect of OCA-B deletion in mouse T cells on autoimmune diabetes induced by ICI treatment and on immunological control of tumors in the absence and presence of ICIs, as well as to test the abilities of small molecule inhibitors. Methods included spatial transcriptomics to assess human *POU2AF1* in the context of T1D, assessment of glucose levels and tumor size, flow cytometry and histology to assess degrees of infiltration and the qualitative nature of the cells, and transcriptional reporter, nanoBRET, EMSA and nanoDSF measurements of small molecule efficacy. Sample sizes (n=3–12) were determined to be sufficient for the type of assay and statistical analysis. Excepting histological scoring, investigators were not blinded when conducting or analyzing the experiments outlined in this study. Mice were randomly assigned to treatment groups and repeat experiments were performed in both males and females where appropriate (e.g., where tumor engraftment was feasible), with no apparent sex differences.

Spatial transcriptomics

Imaging-based spatial transcriptomics of pancreatic tissue was prepared using the network of Pancreatic Organ Donors with Diabetes (nPOD) donor tissue and the Xenium Prime in situ gene expression platform (10X Genomics) according to the manufacturers protocol. Pancreas sections were obtained from the nPOD donor 6551 (RRID: SCR+014641; https://npod.org/), a 20 year-old male with early (6 months onset) T1D (AAb count: 4) with approval from the University of Florida Institutional Review Board (IRB #201600029). Output data were processed as previously described (*46*). Xenium data were visualized using Xenium Explorer 4 software (v4.0.0).

Laboratory mice

All mice used in this study were non-obese diabetic (NOD) background, with the exception of B16-F10 and MC38 tumor injections which used C57BL/6 mice. *Pou2af1* (*Ocab*) conditional (floxed) mice on the C57BL/6 and NOD backgrounds were generated as described previously (*31, 42*). All animal experiments were approved by the University of Utah Institutional Animal Care and Use Committee (IACUC approval 00001553).

α-PD-1-induced diabetes

250 µg α-PD-1 (clone RMP1-14, Cat# BE0146, Bio X Cell) or rat IgG2a isotype control (Cat# BE0089, Bio X Cell) was intraperitoneally (*i.p.*) administered into NOD.$Ocab^{fl/fl}$ or $Ocab^{fl/fl}$;CD4-Cre every 4 days as indicated. Antibody was diluted in PBS for injection of 200 µL per mouse.

Histology

Salivary glands and lacrimal glands were isolated and fixed in 10% formalin. After 24-72 hr, tissues were transferred to 70% ethanol and embedded in paraffin, sectioned at 5~7 µm though the middle of

401 the tissue along the long axis, and H&E staining was performed. Slides were examined and imaged
402 using an Olympus BX53 microscope with UPlanFL objectives, Olympus DP73 camera, and Olympus
403 cellSens imaging software. For lacrimal glands, inflammation was assessed by quantifying the
404 percentage of the gland area with inflammation. For salivary glands, leukocytic number per 10× field
405 was quantified by counting the numbers of inflammatory foci and dividing by the number of 10× fields
406 of the whole tissue.

407

408 **Secondary lymphoid organ and tumor harvest**

409 Spleens and lymph nodes were ground and filtered through a 70 µm nylon cell strainer (VWR #76327-
410 100). Red blood cells were removed by Ammonium-Chloride-Potassium (ACK) lysis buffer (10 mM
411 $KHCO_3$, 150 mM NH_4Cl, and 0.1 mM Na_2EDTA). Immune cells were recovered from MC38 tumors
412 using a published method (*89*) in which tumors were manually disrupted by grinding between the
413 frosted end of slide glass in a 6-well plate with 3 mL of PBS plus 4% FBS, and filtered through a 40
414 µm nylon cell strainer (VWR #76327-098). 9495 tumors were mechanically disrupted in 6-well-plate
415 and digest in RPMI media containing 16mg/mL collagenase D (Sigma-Aldrich #11088858001) and
416 10mg/mL Dnase (Sigma-Aldrich #10104159001) at 37°C in CO_2 incubator for 45 minutes and filtered
417 through a 40 µm nylon cell strainer, spined in 37.5% percoll gradient, and red blood cells (RBCs) were
418 lysed to produce single-cell suspensions.

419

420 **Pancreatic islet harvest**

421 Lymphocytes were isolated based on a protocol from Jing et al. (*90*). Pancreata were harvested and
422 perfused with collagenase 4 (Worthington #LS004188) at 37°C, and islets were picked using a 10 µL
423 pipette. Islet single-cell suspensions were obtained by vortexing in cell dissociation buffer
424 (ThermoFisher Scientific #13151014).

425

426 **Flow cytometry**

427 Single-cell samples were stained with antibodies (1:100 diluted in FACS buffer) for flow cytometric
428 analysis. For intracellular staining, cells were cultured in RPMI1640 (ThermoFisher Scientific
429 #11875093) supplemented with 10% FBS, 1% penicillin/streptomycin (ThermoFisher Scientific
430 #15140122) and 1% GlutaMAX (ThermoFisher Scientific #35050061), 1 µL/mL Brefeldin A (BD
431 Biosciences #555029), 50 ng/mL phorbol 12-myristate 13-acetate (Sigma-Aldrich #P1585) and 1
432 ug/mL ionomycin (Sigma-Aldrich #I0634) for 4 hr. Cells were stained for surface markers and fixed
433 using Cytofix/Cytoperm (BD Biosciences #554714) following the manufacture's protocol, and
434 resuspended in Perm/Wash buffer for intracellular cytokine staining. For intranuclear staining, cells
435 were stained for surface markers, fixed using the Foxp3/Transcription Factor Staining Buffer Kit
436 (ThermoFisher Scientific #00-5523-00) and stained for intranuclear markers. Flow cytometry was
437 performed using a BD Fortessa (BD Biosciences). Data analysis was performed using FlowJo
438 software (BD Biosciences).

439

440 **Cell lines**

441 Mouse MC38 cell line was a gift from Ryan O'Connell (University of Utah). B16-F10 cells were a gift
442 from the lab of Matthew A. Williams (University of Utah). MC38 cells were grown in DMEM
443 (ThermoFisher Scientific #11965092) supplemented with 10% FBS, 1% penicillin/streptomycin, 1%
444 MEM-NEAA (ThermoFisher Scientific #11140050) and 1% HEPES-Cl pH 7.3 (ThermoFisher Scientific
445 #15630130). B16-F10 cells were grown in DMEM supplemented with 10% FBS and 1%
446 penicillin/streptomycin. NOD 9495 cells were grown similar to a prior report (*54*) in DMEM (no
447 glutamine, no sodium pyruvate, ThermoFisher Scientific #11960044) supplemented with 10% FBS
448 (ThermoFisher Scientific #A5256701) 1% penicillin/streptomycin, 1% sodium pyruvate, 1% 100×
449 MEM-NEAA, 1% GlutaMAX (ThermoFisher Scientific #35050061). SupT1 human T lymphoblast cells
450 were grown in RPMI1640 supplemented with 5% FBS, 5% calf serum (Sigma), 1%
451 penicillin/streptomycin and 1% GlutaMAX at 37°C with 5% CO_2.

452

453 **Tumor cell line engraftment**

454 All tumor experiments used 6- to 10-week-old C57BL/6 or 6-8-week-old NOD background mice. For
455 injections of B16-F10 and MC38, after trypsinization, cultured tumor cells were resuspended in PBS
456 and 1×10^6 and 5×10^5 tumor cells were *s.c.* injected into the hind flank of mice, respectively. MC38
457 tumor-bearing mice were treated with 300 µg α-PD-1 or PBS control. For the injection of NOD 9495
458 tumor line, after trypsinization, cultured tumor cells were resuspended in PBS and 1.5×10^6 tumor cells
459 were *s.c.* injected into the hind flank of mice as described (*54*). To treat tumor-bearing NOD mice
460 while minimizing diabetes induction, 200 µg α-PD-1 or PBS control was used. To minimize
461 complications from hyperglycemia, mice were administered insulin pellets when blood glucose levels
462 reached ≥250 mg/dL for two consecutive days.

463

464 **Small molecules**

465 Synthesis of DB1033, DB2232, DB2658, DB2379, DB2559, and DB2385 has been previously
466 reported (*91*). All compounds were dissolved in 100% DMSO and stored at 5mM at -80°C for later
467 use. For cell-based assays, stock solutions or DMSO vehicle controls were diluted in culture media.
468 For EMSA, compounds were diluted in 0.6X buffer D (*92, 93*). For mouse injections, sterile PBS was
469 used to dissolve the compounds.

470

471 **Generation of SupT1 luciferase reporter cell lines**

472 Reporter constructs were generated using a modified secreted nano-luciferase vector, pNL2.3
473 (Promega #N108A), with the hygromycin resistance cassette replaced with puromycin resistance
474 cassette (to generate pNL2.3-Puro). Gene blocks (Integrated DNA Technologies) were synthesized
475 containing 5 canonical Oct1 binding motifs (ATGCAAAT, 5×Oct) or mutant motifs (CAAACTAC, 5×Mut)
476 upstream of a minimal CMV promoter. Gene blocks were subcloned into the multiple cloning site of
477 pNL2.3-Puro using EcoRV and HindIII restriction sites. To generate stable transfectants, human
478 SupT1 cells were electroporated using Neon (ThermoFisher Scientific) with 1 µg of either the pNL2.3-
479 Puro empty-vector (EV), pNL2.3-Puro 5×Oct (5×Oct), or pNL2.3-Puro 5×Mut (5×Mut) construct.
480 Electroporation parameters were: 1700 V, 10 milliseconds, ×3 pulses. Electroporated cells were

481 allowed to recover for 2 days, then selected for stable DNA integration and expanded in complete
482 media containing 1 μg/mL puromycin (ThermoFisher Scientific #A1113803) for 2 weeks. Cells were
483 then single cell-cloned by limited dilution in complete media containing 1 μg/mL puromycin.

484

485 **SupT1 OCA-B activity assays**

486 1.0×10^5 5×Oct and 5×Mut reporter cells were seeded into wells of 96-well plates were cultured in 100
487 μL complete RPMI in complete medium with serially diluted compounds for 18-20 hr. Supernatant was
488 collected and mixed with 1:50 buffer-diluted Nano-Glo luciferase substrate (Cat# N1110, Promega).
489 Luminescence was measured using a Modulus Microplate Multimode Reader (Promega).

490

491 **In vivo treatment of PD-1 blockade-induced diabetes**

492 NOD.*Ocab*$^{fl/fl}$ and NOD.*Ocab*$^{fl/fl}$;CD4-Cre mice were *i.p.* administered with α-PD-1 and 15 mg/kg of
493 DB1033 or DB2232 was administered *i.p.* to the mice on day 0, 4, 8, and 12, and one additional dose
494 of DB1033 or DB2232 on day 11. Mice were sacrificed on day 24.

495

496 **Construction and purification of recombinant Oct1 DNA binding domain Oct1-fusion proteins**

497 A cDNA for the Oct1 DNA binding domain (comprising POU_S and POU_H subdomains) fused to OCA-$_{B1-}$
498 $_{44}$ was ordered from IDT and included an N-terminal 6-His, consecutive C-terminal Twinstrep and
499 FLAG tags. the cDNAs were cloned into the pET28a vector (Invitrogen) between the *Nco*I and *Hind*III
500 sites. The plasmids were transformed into Rosetta 2 (DE3) pLysS competent cells (Sigma) using 50
501 μg/ml kanamycin as a selectable marker. Protein was expressed using 1 mM IPTG (Sigma) at 37°C
502 for three hr. The cells were lysed in buffer containing 20 mM HEPES, pH 7.4 (Sigma), 300 mM NaCl
503 (Sigma), 5% glycerol (Sigma) and 1 mM DTT (ThermoFisher Scientific) containing EDTA-free
504 protease inhibitor cocktail (Sigma) at 2X concentration. Protein was bound to a Histrap column
505 (Cytiva) using the same buffer and eluted with buffer containing 400 mM imidazole (Sigma). The
506 protein was further purified by size exclusion chromatography on a Superdex increase 75 10/300 GL
507 column (Cytiva.inc). The column was loaded using PBS containing 1 mM DTT. The protein was
508 analyzed on 12% SDS-PAGE gel visualized by Coomassie staining.

509

510 **NanoBRET**

511 The NanoBRET donor plasmid was made by cloning nLuc in-frame with the N-terminus of full-length
512 human Oct1 between the *Nco*I and *Xba*I restriction sites of pACE-MAM2 (Geneva Biotech). The
513 acceptor plasmid was made by cloning full-length human OCA-B containing a C-terminal HaloTag into
514 pHTC vector (Promega) between the *Eco*RI and *Xho*I sites. nanoBRET was performed using the
515 NanoBRET protein:protein interaction kit (Promega) following the manufacturer protocol. Briefly, 2×10^6
516 293T cells were plated in 6-well plates were transfected with a total of 2 μg of donor plus acceptor
517 plasmid at a ratio of 1:100. After 24 hr, cells were harvested and counted. 2×10^5 resuspended cells
518 were seeded into the wells of 96-well plates using DMEM lacking phenol red (ThermoFisher Scientific)
519 containing 10% FBS. After 1 hr, DB1033 or DMSO vehicle control were also added at the indicated

concentrations in biological triplicate. After 24 hr, the Nanuck substrate and Halo-ligand were added before measuring BRET ratio using plate reader (Spectromax iD5, Molecular Devices Inc.). The miliBRET ratio was plotted with respect to the DB1033 concentration.

EMSA

Published protocols (*92, 93*) were used for EMSA. The octamer sequence probe was 5' labeled with Cy-5 and used at a final concentration of 40 nM. The probe was incubated with 10 nM Oct1-OCA B chimeric protein ±equimolar OCA B (1-44) peptide over ice for 15 min prior to the addition of 100 nM-400 nM DB1033, then further incubated over ice for another 15 min. Reaction mixtures were electrophoresed through 6% native polyacrylamide gels. Images were collected using a Molecular Dynamics Typhoon scanner using the Cy-5 fluorescence filter.

NanoDSF

Tryptophan fluorescence at 330 nm and 350 nm were simultaneously monitored over a temperature range from 25°C to 95°C using a NanoTemper Technologies nanoDSF instrument with an excitation wavelength of 280 nm based on published procedures (*94*). The Oct1-OCA B chimeric protein complexed with double-stranded DNA containing an Oct1-OCA-B binding site was incubated on ice for 15 min. Protein lacking DNA was used as a control. The effect of DB1033 compound or DMSO control on the protein DNA complex were measured by comparing the melting point of the protein/DNA complex ±DB1033 compound. 10 µl from each sample was loaded into each capillary avoiding any air bubbles. The fluorescence intensity ratio and its first derivative were calculated with the manufacturer's software (PR.ThermControl, version 2.1.2). The smoothened curves and the first derivative were plotted in using Microsoft Excel software. The peak from the first-order derivative indicates the melting temperature of the sample protein sample.

Statistical analyses

Two-tailed student's t-tests were used to determine statistical differences in experiments with pairwise comparison of data points between two groups. Two-way ANOVA analyses were used to determine statistical differences in the tumor growth curves. Survival curves used a Mantel-Haenszel test to calculate hazard ratio and a Mantel-Cox test to calculate statistical significance. All error bars represent ±standard deviations unless otherwise noted. For tumor growth assays, error bars denote ±SEM. For all other experiments, error bars denote ±standard deviation. For all figures, ns (not significant), $p > 0.05$; *, $p \leq 0.05$; **, $p \leq 0.01$; ***, $p \leq 0.001$; ****, $p \leq 0.0001$.

553 **FIGURE LEGENDS**

554 **Fig. 1. POU2AF1 labels pathogenic T cells in the setting of human T1D. (A)** 10X Xenium image of
555 a pancreatic islet from a 20-year-old human patient with early T1D. *CHGA* (red), *CD8A* (purple),
556 *MSFA1* (orange) and *POU2AF1* (green) transcripts are annotated. Cells were identified by imputation
557 as CD8+ T cells (yellow), B cells (green), or islet endocrine cells (gray). Yellow arrows highlight
558 *POU2AF1*-expressing $CD4^+$ T cells and red arrows highlight *POU2AF1*-expressing B cells. (**B**) Data
559 from pLN sections of the same individual. *CD3E* (white), *CD4* (green), *CD8A* (yellow), *MS4A1*
560 (magenta), *POU2AF1* (blue). Yellow arrows highlight T cells that also express *POU2AF1*. (**C**) Detail
561 from the white box in the right panel shown in (B), with a slightly different transcript annotation color
562 scheme: *CD3E* (white), *CD4* (green), *CD8A* (yellow), *MS4A1* (black), *POU2AF1* (red). B cells
563 expressing *POU2AF1* were abundant and are not highlighted.

564

565 **Fig. 2. OCA-B deletion in T cells confers protection against PD-1 blockade-induced diabetes in**
566 **NOD mice. (A)** Schematics of experimental workflow for monitoring α-PD-1-induced autoimmune
567 diabetes in 8-week-old NOD male *Ocab*$^{fl/fl}$ and *Ocab*$^{fl/fl}$;CD4-Cre injected with α-PD-1, and monitoring
568 pre-diabetic mice at short timepoints (day 5) after a single α-PD-1 injection. **(B)** Kaplan-Meier plot of
569 diabetes-free 8-week-old NOD male *Ocab*$^{fl/fl}$ (n=7) and *Ocab*$^{fl/fl}$;CD4-Cre (n=7) mice. 250 μg α-PD-1
570 was administered by *i.p.* injection on day 0, 4, 8 and 12. Blood glucose levels were measured every 1-
571 2 days, with mice considered diabetic if glucose rose above 250 mg/dL over two consecutive days.
572 **(C)** Blood glucose levels of individual mice from (B). **(D)** Islets were prepared from 8-week-old treated
573 knockout and littermate control female mice 5 days after one dose of α-PD-1 antibody for flow
574 cytometry. Representative flow cytometry plots depicting total infiltrating $CD45^+$ leukocytes for control
575 and knockout mice. (**E**) Quantification of total infiltrating $CD45^+$ islet leukocyte flow cytometry data
576 from NOD.*Ocab*$^{fl/fl}$ (n=7) and NOD.*Ocab*$^{fl/fl}$;CD4-Cre mice (n=8). (**F**) Representative flow cytometry
577 plots depicting $CD4^+$ and $CD8^+$ islet T cells. Cells were pre-gated on $CD45^+CD3\varepsilon^+$. (**G**) Quantification
578 of $CD8^+/CD4^+$ ratio from NOD.*Ocab*$^{fl/fl}$ (n=7) and NOD.*Ocab*$^{fl/fl}$;CD4-Cre mice (n=8). (**H**)
579 Representative flow cytometry plots showing CD62L and CD11a expressions of islet-infiltrating $CD8^+$
580 T cells. (**I**) Quantification of activated $CD62L^-CD11a^+CD8^+$ T cells from NOD.*Ocab*$^{fl/fl}$ (n=7) and
581 NOD.*Ocab*$^{fl/fl}$;CD4-Cre mice (n=8). (**J**) Representative flow cytometry plots depicting PD-1-expressing
582 $CD8^+$ islet-infiltrating T cells. Cells were pre-gated on $CD3\varepsilon^+CD8^+$. (**K**) Quantification of the
583 percentage of PD-1^+ T cells among $CD8^+$ T cells from NOD.*Ocab*$^{fl/fl}$ (n=7) and NOD.*Ocab*$^{fl/fl}$;CD4-Cre
584 mice (n=8). (**L**) Representative flow cytometry plots depicting the percentage of islet $SLAMF6^+CD39^-$
585 T_{PEX} and $SLAMF6^-CD39^+$ T_{EX}. Cells were pre-gated on PD-1^+CD8^+. (**M**) Quantification of flow
586 cytometry data for the percentages of T_{EX} among $CD8^+$PD-1^+ and total cells in islets from
587 NOD.*Ocab*$^{fl/fl}$ (n=7) and NOD.*Ocab*$^{fl/fl}$;CD4-Cre mice (n=8).

588

589 **Fig. 3. OCA-B in T cells is dispensable for anti-tumor immunity in C57BL/6 mice. (A)** 5×10^5
590 MC38 tumor cells were *s.c.* implanted into the hind flanks of female C57BL/6 *Ocab*$^{fl/fl}$ and
591 *Ocab*$^{fl/fl}$;CD4-Cre mice. 300 μg α-PD-1 (or PBS) was administered *i.p.* on day 4, 7 and 10. Tumor
592 sizes were measured every 3-4 days, and mice were euthanized at end point (day 23) or upon tumor
593 size reaching 2 cm in any direction. *Ocab*$^{fl/fl}$+PBS (n=7), *Ocab*$^{fl/fl}$;CD4-Cre+PBS (n=11), *Ocab*$^{fl/fl}$+α-PD-
594 1 (n=8), and *Ocab*$^{fl/fl}$;CD4-Cre+α-PD-1 (n=8). **(B)** Mean tumor sizes from (A) are shown. *Ocab*$^{fl/fl}$+PBS
595 (n=7), *Ocab*$^{fl/fl}$;CD4-Cre+PBS (n=11), *Ocab*$^{fl/fl}$+α-PD-1 (n=8), and *Ocab*$^{fl/fl}$;CD4-Cre+α-PD-1 (n=8). **(C)**

596 Quantification of flow cytometry data showing the percentage of CD45.2$^+$ tumor-infiltrating leukocytes
597 (TILs) in MC38 TMEs from α-PD-1 antibody-treated *Ocab*$^{fl/fl}$ (n=6) and *Ocab*$^{fl/fl}$;CD4-Cre (n=6) mice on
598 day 23 or upon tumor size reaching 2 cm in any direction. **(D)** Quantification of flow cytometry data
599 showing the ratio of CD8$^+$ to CD4$^+$ T cells in the TME. **(E)** Representative flow cytometry plots of
600 endpoint TME CD4$^+$ and CD8$^+$ T cell SLAMF6 and CD39 expression. *Ocab*$^{fl/fl}$ (n=6) and *Ocab*$^{fl/fl}$;CD4-
601 Cre (n=5) tumor-bearing mice were treated with α-PD-1 antibodies. (**F**) Quantification of flow
602 cytometry data for endpoint TME CD4$^+$ and CD8$^+$ T cell SLAMF6 and CD39 expression from *Ocab*$^{fl/fl}$
603 (n=6) and *Ocab*$^{fl/fl}$;CD4-Cre (n=5) mice. (**G**) Representative flow cytometry data for endpoint TME
604 CD8$^+$ and CD4$^+$ T cell TIM-3 expression. (**H**) Quantification of flow cytometry data at endpoint showing
605 TME CD4$^+$ and CD8$^+$ T cell TIM-3 expression from *Ocab*$^{fl/fl}$ (n=6) and *Ocab*$^{fl/fl}$;CD4-Cre (n=6) mice.

606

607 **Fig. 4. OCA-B in T cells is dispensable for anti-tumor immunity in NOD mice. (A)** 1.5×10^6 9495
608 tumor cells were *s.c.* implanted into the hind flanks of male NOD.*Ocab*$^{fl/fl}$ and NOD.*Ocab*$^{fl/fl}$;CD4-Cre
609 mice. Three doses of 200 µg α-PD-1 (or PBS vehicle control) were *i.p.* administered on day 10, 14
610 and 18. Tumor sizes were measured during different stages of tumor growth. *Ocab*$^{fl/fl}$+PBS (n=6),
611 *Ocab*$^{fl/fl}$;CD4-Cre+PBS (n=7), *Ocab*$^{fl/fl}$+α-PD-1 (n=8), and *Ocab*$^{fl/fl}$;CD4-Cre+α-PD-1 (n=12). **(B)**
612 Quantification of flow cytometry data for the percentage of CD45$^+$ infiltrating cells in the TME from α-
613 PD-1 antibody-treated control *Ocab*$^{fl/fl}$ (n=9) and littermate experimental *Ocab*$^{fl/fl}$;CD4-Cre (n=5) mice.
614 **(C)** Representative flow cytometry plots depicting CD4$^+$ and CD8$^+$ TME T cells from α-PD-1 antibody-
615 treated control NOD.*Ocab*$^{fl/fl}$ and littermate experimental NOD.*Ocab*$^{fl/fl}$;CD4-Cre mice. Cells were pre-
616 gated using α-CD3 staining. (B) Quantification of flow cytometry data depicting the percentage of
617 CD4$^+$ and CD8$^+$ T cells in the TME from NOD.*Ocab*$^{fl/fl}$ (n=9) and NOD.*Ocab*$^{fl/fl}$;CD4-Cre mice (n=5). (**E**)
618 Representative flow cytometry plots depicting relative percentages of SLAMF6$^-$ and CD39$^-$expressing
619 infiltrating CD8$^+$PD-1$^+$ T cells. (**F**) Quantification of PD-1$^+$SLAMF6$^+$CD39$^-$CD8$^+$ T_{PEX} and PD-
620 1$^+$SLAMF6$^-$CD39$^+$CD8$^+$ T_{EX} among PD-1$^+$CD8$^+$ T cells in the TME from NOD.*Ocab*$^{fl/fl}$ (n=9) and
621 NOD.*Ocab*$^{fl/fl}$;CD4-Cre mice (n=5). (**G**) Representative flow cytometry plots depicting TIM-3 levels in
622 infiltrating CD8$^+$ T cells. (**H**) Quantification of TIM-3$^+$ cells among CD8$^+$ T cells in the TME from
623 NOD.*Ocab*$^{fl/fl}$ (n=9) and NOD.*Ocab*$^{fl/fl}$;CD4-Cre mice (n=5). In (panels C-H), one data point from
624 NOD.*Ocab*$^{fl/fl}$ was removed because of low cell numbers.

625

626 **Fig. 5. OCA-B cellular inhibition by small molecule DNA minor groove binders** (**A**) Oct1:OCA-
627 B:DNA co-crystal structure (*45*) showing two targeting approaches: a peptide that mimics the key
628 OCA-B alpha helix involved in downstream effector functions (top lightning bolt) (*42*), and a minor
629 groove DNA binding molecule with potential to disrupt the unstructured Oct1 linker domain between
630 the two DNA binding subdomains (bottom lightning bolt). (**B**) OCA-B immunoblots from SupT1 and
631 Jurkat T cell lines (lanes 3-4). Isolated mouse primary thymocyte and 293T cell lysates were also
632 used as positive and negative controls, respectively (lanes 1-2). Histone H3 is shown as a loading
633 control. (**C**) Schematic for OCA-B luciferase reporter cell lines. SupT1 cells were stably transfected
634 with reporter plasmids containing five tandem canonical Oct1:OCA-B binding sites linked to a CMV
635 promoter upstream of secreted nLuc (5×Oct) or an identical plasmid except containing mutant binding
636 sites used to determine nonspecific effects (5×Mut). Cells were selected with puromycin, single-cell
637 cloned, and individual clones used subsequently. (**D**) Luciferase activity of pNL2.3 empty vector
638 ("EV"), 5×Oct, or 5×Mut reporter lines. Cells were incubated for 18 hr after plating. n=4 biological
639 replicate platings for each cell line. (**E**) Luciferase expression kinetics of cultured 5×Oct cells. A

640 timecourse of 2-46 hr is shown. Averages are shown from n=5 biological replicate platings. Trendline
641 shows logistic growth fit. (**F**) Inhibition of cellular OCA-B activity by an escalating dose of the small
642 molecule DB1033. Values from 5×Oct and 5×Mut clones were normalized to one another in the
643 absence of DB1033. Averages are shown across n=6 biological replicate platings. Red curve shows
644 the "5×Oct" fit to the Hill equation. Asterisks denote results from two-tailed student T-test comparing
645 5×Oct and 5×Mut at the highest concentration. (**G**) Chemical structure of DB1033. (**H**) Molecular
646 docking of DB1033 to canonical octamer B-form DNA. Red shows water molecules. DB1033 is shown
647 in purple. Red/underlined nucleotides show the minor groove bases contacted by DB1033 docked
648 with the lowest free energy. (**I**) Wireframe model showing DB1033 bound to the minor groove AAAT
649 site. Hydrogen bond interactions formed between DB1033 and the minor groove AAAT site are shown
650 with dashed lines.

651

652 **Fig. 6. DB1033 inhibits OCA-B-Oct1-DNA complex formation.** (**A**) Schematics of full-length Oct1
653 tagged with N-terminal nLuc and full-length OCA-B with a C-terminal HaloTag used for nanoBRET. (**B**)
654 Quantification of nanoBRET signal obtained by co-transfecting the 293T cells with the constructs
655 shown in A in the presence of increasing concentrations of DB1033. An average of n=3 biological
656 replicate platings is shown. DB1033 was applied at the indicated concentrations 1 hr after seeding the
657 cells and cells were collected after a further 24 hr.(**C**) Schematics of the C-terminally Twinstep-tagged
658 Oct1 DNA-binding domain ($Oct1_{DBD}$) and full-length OCA-B with a C-terminal FLAG tag used in
659 EMSA. (**D**) Cy5-DNA scan of native PAGE EMSA showing DNA-$Oct1_{DBD}$ complex formation with OCA-
660 B, and concentration-dependent inhibition by DB1033. (**E**) A schematic of the $Oct1_{DBD}$:OCA-B_{1-44}
661 fusion protein engineered for nanoDSF. (**F**) Structure of the OCA-B_{1-44}-$Oct1_{DBD}$ complex predicted
662 using Alphafold 3. Cyan: OCA-B_{1-44} peptide. Green: $Oct1_{DBD}$ peptide. Dark blue shows the Oct1:DNA
663 structure derived from X-ray crystallography (*45*). (**G**) nanoDSF measurement of the thermal stability
664 of 10 μM $Oct1_{DBD}$-OCA-B_{1-44} chimeric protein with or without added canonical octamer DNA. First
665 derivative is shown below. (**H**) First derivative nanoDSF data in the presence of DNA and the
666 presence (above) or absence (below) of 100 μM DB1033.

667

668 **Fig. 7. DB1033 inhibits PD-1 blockade-induced diabetes in NOD mice.** (**A**) Kaplan-Meier plot of
669 diabetes-free mice in 8-week-old male NOD.*Ocab*$^{fl/fl}$ treated with PBS (n=4), NOD.*Ocab*$^{fl/fl}$ treated with
670 DB1033 (n=4) and NOD.*Ocab*$^{fl/fl}$;CD4-Cre mice treated with PBS (n=4). Black arrows: 250 μg α-PD-1
671 and 15 mg/kg *i.p.* injections on day 0, 4, 8, 12. Grey arrow: an additional *i.p.* injection of 15 mg/kg
672 DB1033 was administered on day 11. (**B**) Average blood glucose levels of mice in (A). (**C**) Mouse
673 body weight on day 24 of the experiment described in (A). (**D**) Example H&E images of lacrimal and
674 salivary gland sections harvested from 8-week-old male NOD mice injected with α-PD-1 antibodies in
675 (A). (**E**) Quantification of the histological scoring described in (D). NOD.*Ocab*$^{fl/fl}$ treated with PBS
676 (n=4), NOD.*Ocab*$^{fl/fl}$ treated with DB1033 (n=4) and NOD.*Ocab*$^{fl/fl}$;CD4-Cre mice treated with PBS
677 (n=4). Histological scoring was conducted by individuals blinded to treatment group.

678

679 **Supplemental Figure Legends**

680 **Fig. S1. OCA-B deletion in T cells protects NOD mice from spontaneous and PD-1 blockade-**
681 **induced diabetes.** (**A**) Kaplan-Meier plot of diabetes-free mice in 12-week-old female littermate

control NOD.*Ocab*$^{fl/fl}$ (n=5) or experimental NOD.*Ocab*$^{fl/fl}$;CD4-Cre (n=6) mice receiving 250 μg α-PD-1 antibody injections on day 0, 4, 8, 12, and 16, indicated by black arrows. Spontaneous T1D was monitored in NOD.*Ocab*$^{fl/fl}$ (n=5) and NOD.*Ocab*$^{fl/fl}$;CD4-Cre (n=5) mice receiving PBS. (**B**) Blood glucose levels were plotted from individual mice receiving α-PD-1 antibody in (A). (**C**) Flow cytometry plots showing percentages of CD8$^+$PD-1$^+$ islet T cells collected from 12-week-old mice 6 days post-α-PD-1 treatment. (**D**) Quantification of PD-1$^+$ T cells among CD8$^+$ T cells from islets of *Ocab*$^{fl/fl}$ (n=3) and *Ocab*$^{fl/fl}$;CD4-Cre mice (n=5). (**E**) Flow cytometry plots showing percentages of SLAMF6$^+$CD39$^-$ and SLAMF6$^-$CD39$^+$ among CD8$^+$PD-1$^+$ T cells in islets collected from 12-week-old mice 6 days post-α-PD-1 treatment. (**F**) Quantification of flow cytometry data in (E) from *Ocab*$^{fl/fl}$ (n=3) and *Ocab*$^{fl/fl}$;CD4-Cre mice (n=5). Percentages of CD8$^+$PD-1$^+$SLAMF6$^-$CD39$^+$ among total islet cells were shown. (**G**) Flow cytometry plots showing percentages of SLAMF6$^+$CD39$^-$ and SLAMF6$^-$CD39$^+$ among CD4$^+$PD-1$^+$ T cells in islet collect from 12-week-old mice 6 days post-α-PD-1 treatment. (**H**) Quantification of flow cytometry data in (**G**) from NOD.*Ocab*$^{fl/fl}$ (n=3) and NOD.*Ocab*$^{fl/fl}$;CD4-Cre mice (n=5).

Fig. S2. OCA-B deletion in T cells results in the accumulation of CD62L^{hi} T_{PEX} in pancreatic islets. (**A**) Flow cytometry plots showing percentages of T_{PEX} (SLAMF6$^+$CD39$^-$) and T_{EX} (SLAMF$^-$CD39$^+$) in islets collected from NOD 8-week-old males without α-PD-1 treatment. (**B**) Quantification of percentages of T_{PEX} (SLAMF6$^+$CD39$^-$) and T_{EX} (SLAMF$^-$CD39$^+$) among total cells from islets of *Ocab*$^{fl/fl}$ (n=3) and *Ocab*$^{fl/fl}$;CD4-Cre mice (n=5). (**C**) Flow cytometry plots showing expressions of CD62L and CD39 from mice in Fig. 2. Cells were pre-gated on CD8$^+$PD-1$^+$. (**D**) Quantification of flow cytometry data for the percentage of CD62L$^+$$T_{PEX}$, conventional CD62L$^-$ T_{PEX} and CD39$^+$ T_{EX} in islets from NOD.*Ocab*$^{fl/fl}$ (n=7) and NOD.*Ocab*$^{fl/fl}$;CD4-Cre mice (n=8).

Fig. S3. OCA-B deletion in T cells leaves B16F10 tumor growth and unaltered. Growth of *s.c.* B16F10 tumors in C57BL/6 mice sufficient (blue, *Ocab*$^{fl/fl}$, n=3) and deficient (red, *Ocab*$^{fl/fl}$;CD4-Cre, n=3) for T cell-expressed OCA-B. No α-PD-1 was provided.

Fig. S4. NOD tumor additional data. (A) Kaplan-Meier plot of another cohort of diabetes-free mice performed with the same experimental procedures as in Figure 3. *Ocab*$^{fl/fl}$ (n=14) and *Ocab*$^{fl/fl}$;CD4-Cre (n=9). **(B-E)** Flow cytometric analysis was performed on tumors harvested from mice with similar experiment procedures described in Fig. 4A. Representative plots and quantifications of CD4$^+$ and CD8$^+$ effector (CD44$^+$CD62L$^-$) T cells, and exhausted (PD-1$^+$) CD4$^+$ and CD8$^+$ T cells are shown.

Fig. S5. Effect of staurosporine on luciferase-based transcription activity in SupT1 cells. A dose curve of staurosporine is shown using both the 5×Oct and 5×Mut cell lines. Trendlines show the fit to the Hill equation.

Fig. S6. OCA-B cellular inhibition by additional small molecule DNA minor groove binders. (**A**) Inhibition of cellular OCA-B activity by DB2232. Blue datapoints represent control measurements of nonspecific transcription measured in 5×Mut cells. Red datapoints represent experimental

722 measurements from the 5×Oct line. Luciferase values were normalized to 1.0 in the absence of
723 DB2232. Trendlines show the fit to the Hill equation. (**B-H**) Similar data for additional molecules.
724 5×Mut cells were used for panels (F,G,H). Cytotoxicity was measured using viable cell counts for
725 panels (B,C,D,E).

726 **Fig. S7. Additional nanoDSF validation data and DB2232 effect on PD-1 blockade-induced**
727 **diabetes in NOD mice. (A)** Image of a 12% SDS-polyacrylamide gel loaded with the purified
728 recombinant chimeric Oct1 DBD-OCA-B protein and stained with Coomassie blue. Molecular weight
729 makers are shown at left as a standard. **(B)** Size exclusion chromatography elution profile using the
730 Oct1-OCA-B chimera. **(C)** EMSA using the Oct1-OCA-B chimera and Cy5-labeled prefer octamer
731 consensus DNA. **(D)** Kaplan-Meier plot of diabetes-free mice in 8-week-old male NOD.*Ocab*$^{fl/fl}$ mice
732 treated with PBS (n=7), NOD.*Ocab*$^{fl/fl}$ mice treated with DB2232 (n=4) and NOD.*Ocab*$^{fl/fl}$;CD4-Cre
733 mice treated with PBS (n=7). Black arrows: 250 µg α-PD-1 and 15 mg/kg *i.p.* injections on day 0, 4, 8,
734 12. Grey arrow: an additional *i.p.* injection of 15 mg/kg DB2232 was administered on day 11. **(E)**
735 Average blood glucose levels of mice in (D). **(F)** Body weight of mice on day 24 of the experiment
736 described in (D).

Acknowledgements

We thank R. O'Connell and M. Williams for MC38 and B16F10 cells, A. Young for 9495 cells, and O. Pornillos for use of nanoDSF instrumentation. We thank O. Allen, B. Dalley and the University of Utah High-Throughput Genomics Core facility. We thank J. Marvin and the University of Utah Flow Cytometry Core facility. We acknowledge the Huntsman Cancer Institute Cancer Center Support Grant (CCSG). This work was supported by grants from the National Institutes of Health/National Institute of Allergy and Infectious Diseases (R01AI162929), the Praespero Autoimmune Fund (Canada), and an internal seed grant from the Huntsman Cancer Institute Genomics, Epigenetics and Metabolism (GEM) program to DT. Additional support was provided by National Institutes of Health grant T32 DK108736 (MAM-S) and National Institutes of Health grant P01 AI042288 (TMB). This research was performed with the support of the Network for Pancreatic Organ donors with Diabetes (nPOD; RRID:SCR_014641), a collaborative type 1 diabetes research project supported by Breakthrough T1D and The Leona M. & Harry B. Helmsley Charitable Trust (Grant#3-SRA-2023-1417-S-B). The content and views expressed are the responsibility of the authors and do not necessarily reflect the official view of nPOD. Organ Procurement Organizations (OPO) partnering with nPOD to provide research resources are listed at https://npod.org/for-partners/npod-partners/.

Author contributions

JD, AKM, MAM-S, EPH and PB performed experiments and analyzed data. AY and TMB provided key reagents and methods. KJE acquired images and analyzed data. WDW and AAF synthesized and purified DNA minor groove binding small molecules. DT conceptualized and supervised the study. All authors contributed to the writing of the manuscript.

Competing interests

The authors declare no competing interests.

REFERENCES

1. National Diabetes Statistics Report. *Centers for Disease Control and Prevention*, (2024).
2. I. Ogrotis, T. Koufakis, K. Kotsa, Changes in the Global Epidemiology of Type 1 Diabetes in an Evolving Landscape of Environmental Factors: Causes, Challenges, and Opportunities. *Medicina (Kaunas)* **59**, (2023).
3. G. A. Gregory *et al.*, Global incidence, prevalence, and mortality of type 1 diabetes in 2021 with projection to 2040: a modelling study. *Lancet Diabetes Endocrinol* **10**, 741-760 (2022).
4. D. W. Cooke, L. Plotnick, Type 1 diabetes mellitus in pediatrics. *Pediatr Rev* **29**, 374-384; quiz 385 (2008).
5. D. E. Sutherland *et al.*, Twin-to-twin pancreas transplantation: reversal and reenactment of the pathogenesis of type I diabetes. *Trans Assoc Am Physicians* **97**, 80-87 (1984).
6. F. Vendrame *et al.*, Recurrence of type 1 diabetes after simultaneous pancreas-kidney transplantation, despite immunosuppression, is associated with autoantibodies and pathogenic autoreactive CD4 T-cells. *Diabetes* **59**, 947-957 (2010).
7. Y. Wang, O. Pontesilli, R. G. Gill, F. G. La Rosa, K. J. Lafferty, The role of CD4+ and CD8+ T cells in the destruction of islet grafts by spontaneously diabetic mice. *Proc Natl Acad Sci U S A* **88**, 527-531 (1991).
8. A. Lernmark, H. E. Larsson, Immune therapy in type 1 diabetes mellitus. *Nat Rev Endocrinol* **9**, 92-103 (2013).
9. J. D. Wolchok *et al.*, Final, 10-Year Outcomes with Nivolumab plus Ipilimumab in Advanced Melanoma. *N Engl J Med* **392**, 11-22 (2025).
10. H. A. Tawbi *et al.*, Relatlimab and Nivolumab versus Nivolumab in Untreated Advanced Melanoma. *N Engl J Med* **386**, 24-34 (2022).
11. O. Hamid *et al.*, Safety and tumor responses with lambrolizumab (anti-PD-1) in melanoma. *N Engl J Med* **369**, 134-144 (2013).
12. J. Cortes *et al.*, Pembrolizumab plus Chemotherapy in Advanced Triple-Negative Breast Cancer. *N Engl J Med* **387**, 217-226 (2022).
13. Z. Quandt, A. Young, M. Anderson, Immune checkpoint inhibitor diabetes mellitus: a novel form of autoimmune diabetes. *Clin Exp Immunol* **200**, 131-140 (2020).
14. M. A. Postow, M. K. Callahan, J. D. Wolchok, Immune Checkpoint Blockade in Cancer Therapy. *J Clin Oncol* **33**, 1974-1982 (2015).
15. A. Berti *et al.*, Meta-analysis of immune-related adverse events in phase 3 clinical trials assessing immune checkpoint inhibitors for lung cancer. *Crit Rev Oncol Hematol* **162**, 103351 (2021).
16. T. W. Chen, A. R. Razak, P. L. Bedard, L. L. Siu, A. R. Hansen, A systematic review of immune-related adverse event reporting in clinical trials of immune checkpoint inhibitors. *Ann Oncol* **26**, 1824-1829 (2015).
17. M. A. Postow, R. Sidlow, M. D. Hellmann, Immune-Related Adverse Events Associated with Immune Checkpoint Blockade. *N Engl J Med* **378**, 158-168 (2018).
18. A. Young, Z. Quandt, J. A. Bluestone, The Balancing Act between Cancer Immunity and Autoimmunity in Response to Immunotherapy. *Cancer Immunol Res* **6**, 1445-1452 (2018).
19. G. E. Molina *et al.*, Temporal Trends and Outcomes Among Patients Admitted for Immune-Related Adverse Events: A Single-Center Retrospective Cohort Study from 2011 to 2018. *Oncologist* **26**, 514-522 (2021).
20. A. M. Stamatouli *et al.*, Collateral Damage: Insulin-Dependent Diabetes Induced With Checkpoint Inhibitors. *Diabetes* **67**, 1471-1480 (2018).
21. Z. Quandt, A. Young, A. L. Perdigoto, K. C. Herold, M. S. Anderson, Autoimmune Endocrinopathies: An Emerging Complication of Immune Checkpoint Inhibitors. *Annu Rev Med* **72**, 313-330 (2021).

22. J. C. Osorio *et al.*, Antibody-mediated thyroid dysfunction during T-cell checkpoint blockade in patients with non-small-cell lung cancer. *Ann Oncol* **28**, 583-589 (2017).
23. Z. Quandt *et al.*, Spectrum of Clinical Presentations, Imaging Findings, and HLA Types in Immune Checkpoint Inhibitor-Induced Hypophysitis. *J Endocr Soc* **7**, bvad012 (2023).
24. J. A. Noble, A. M. Valdes, Genetics of the HLA region in the prediction of type 1 diabetes. *Curr Diab Rep* **11**, 533-542 (2011).
25. H. Hu, P. N. Zakharov, O. J. Peterson, E. R. Unanue, Cytocidal macrophages in symbiosis with CD4 and CD8 T cells cause acute diabetes following checkpoint blockade of PD-1 in NOD mice. *Proc Natl Acad Sci U S A* **117**, 31319-31330 (2020).
26. S. A. Long *et al.*, Remodeling T cell compartments during anti-CD3 immunotherapy of type 1 diabetes. *Cell Immunol* **319**, 3-9 (2017).
27. C. Mathieu *et al.*, Toward Disease-Modifying Therapies in Type 1 Diabetes: Focus on Teplizumab. *Diabetes Care* **49**, 365-374 (2026).
28. E. K. Sims *et al.*, Teplizumab improves and stabilizes beta cell function in antibody-positive high-risk individuals. *Sci Transl Med* **13**, eabc8980 (2021).
29. E. L. Ramos *et al.*, Teplizumab and beta-Cell Function in Newly Diagnosed Type 1 Diabetes. *N Engl J Med* **389**, 2151-2161 (2023).
30. S. Zwilling, A. Dieckmann, P. Pfisterer, P. Angel, T. Wirth, Inducible expression and phosphorylation of coactivator BOB.1/OBF.1 in T cells. *Science* **277**, 221-225. (1997).
31. W. Sun *et al.*, OCA-B/Pou2af1 is sufficient to promote CD4+ T cell memory and prospectively identifies memory precursors. *Proc Natl Acad Sci U S A* **121**, e2309153121 (2024).
32. A. Shakya, J. Kang, J. Chumley, M. A. Williams, D. Tantin, Oct1 is a switchable, bipotential stabilizer of repressed and inducible transcriptional states. *J Biol Chem* **286**, 450-459 (2011).
33. A. Shakya *et al.*, Oct1 and OCA-B are selectively required for CD4 memory T cell function. *J Exp Med* **212**, 2115-2131 (2015).
34. E. P. Hughes *et al.*, OCA-B promotes pathogenic maturation of stem-like CD4+ T cells and autoimmune demyelination. *J Clin Invest* **135**, e187862 (2025).
35. M. Nakamura *et al.*, Genome-wide association study identifies TNFSF15 and POU2AF1 as susceptibility loci for primary biliary cirrhosis in the Japanese population. *Am J Hum Genet* **91**, 721-728 (2012).
36. A. Goris *et al.*, New candidate loci for multiple sclerosis susceptibility revealed by a whole genome association screen in a Belgian population. *J Neuroimmunol* **143**, 65-69 (2003).
37. M. Ban *et al.*, Linkage disequilibrium screening for multiple sclerosis implicates JAG1 and POU2AF1 as susceptibility genes in Europeans. *J Neuroimmunol* **179**, 108-116 (2006).
38. D. A. van Heel *et al.*, Inflammatory bowel disease is associated with a TNF polymorphism that affects an interaction between the OCT1 and NF(-kappa)B transcription factors. *Hum Mol Genet* **11**, 1281-1289 (2002).
39. D. S. Cunninghame Graham, A. K. Wong, N. J. McHugh, J. C. Whittaker, T. J. Vyse, Evidence for unique association signals in SLE at the CD28-CTLA4-ICOS locus in a family-based study. *Hum Mol Genet* **15**, 3195-3205 (2006).
40. K. K. Farh *et al.*, Genetic and epigenetic fine mapping of causal autoimmune disease variants. *Nature* **518**, 337-343 (2015).
41. M. T. Maurano *et al.*, Systematic localization of common disease-associated variation in regulatory DNA. *Science* **337**, 1190-1195 (2012).
42. H. Kim *et al.*, Targeting OCA-B/Pou2af1 blocks activated, autoreactive T cells in the pancreas and type-1 diabetes. *J Exp Med* **218**, e20200533 (2021).
43. M. Strubin, J. W. Newell, P. Matthias, OBF-1, a novel B cell-specific coactivator that stimulates immunoglobulin promoter activity through association with octamer-binding proteins. *Cell* **80**, 497-506 (1995).
44. M. Gstaiger, L. Knoepfel, O. Georgiev, W. Schaffner, C. M. Hovens, A B-cell coactivator of octamer-binding transcription factors. *Nature* **373**, 360-362 (1995).

45. D. Chasman, K. Cepek, P. A. Sharp, C. O. Pabo, Crystal structure of an OCA-B peptide bound to an Oct-1 POU domain/octamer DNA complex: specific recognition of a protein-DNA interface. *Genes Dev.* **13**, 2650-2657 (1999).
46. M. Medina-Serpas *et al.*, Spatial transcriptomics from pancreas and local draining lymph node tissue reveals a lymphotoxin-b signature in human type 1 diabetes. *Cell Reports* **(in press)**, (2026).
47. M. J. Ansari *et al.*, The programmed death-1 (PD-1) pathway regulates autoimmune diabetes in nonobese diabetic (NOD) mice. *J Exp Med* **198**, 63-69 (2003).
48. B. T. Fife *et al.*, Insulin-induced remission in new-onset NOD mice is maintained by the PD-1-PD-L1 pathway. *J Exp Med* **203**, 2737-2747 (2006).
49. J. Zhou, J. O. Jin, T. Kawai, Q. Yu, Endogenous programmed death ligand-1 restrains the development and onset of Sjögren's syndrome in non-obese diabetic mice. *Sci Rep* **6**, 39105 (2016).
50. S. Ippolito, G. Di Dalmazi, F. Pani, E. Sabini, P. Caturegli, Distinct Cytokine Signatures in Thyroiditis Induced by PD-1 or CTLA-4 Blockade: Insights from a New Mouse Model. *Thyroid* **31**, 1839-1849 (2021).
51. S. V. Gearty *et al.*, An autoimmune stem-like CD8 T cell population drives type 1 diabetes. *Nature* **602**, 156-161 (2022).
52. A. Martinez-Usatorre, A. Donda, D. Zehn, P. Romero, PD-1 Blockade Unleashes Effector Potential of Both High- and Low-Affinity Tumor-Infiltrating T Cells. *J Immunol* **201**, 792-803 (2018).
53. B. Homet Moreno *et al.*, Response to Programmed Cell Death-1 Blockade in a Murine Melanoma Syngeneic Model Requires Costimulation, CD4, and CD8 T Cells. *Cancer Immunol Res* **4**, 845-857 (2016).
54. A. Young *et al.*, Improving preclinical modeling of irAEs and anti-tumor immunity using syngeneic tumor models in autoimmune-prone NOD mice. *in prep.*, (2026).
55. J. Abramson *et al.*, Accurate structure prediction of biomolecular interactions with AlphaFold 3. *Nature* **630**, 493-500 (2024).
56. X. S. Wu *et al.*, OCA-T1 and OCA-T2 are coactivators of POU2F3 in the tuft cell lineage. *Nature* **607**, 169-175 (2022).
57. A. C. Betzler *et al.*, BOB.1/OBF.1 is required during B-cell ontogeny for B-cell differentiation and germinal center function. *Eur J Immunol* **52**, 404-417 (2022).
58. W. Shi *et al.*, Transcriptional profiling of mouse B cell terminal differentiation defines a signature for antibody-secreting plasma cells. *Nat Immunol* **16**, 663-673 (2015).
59. U. Kim *et al.*, The B-cell-specific transcription coactivator OCA-B/OBF-1/Bob-1 is essential for normal production of immunoglobulin isotypes. *Nature* **383**, 542-547 (1996).
60. D. B. Schubart, A. Rolink, R. G. Kosco-Vilbois, F. Botteri, P. Matthias, B-cell-specific coactivator OBF-1/OCA-B/Bob1 required for immune response and germinal centre formation. *Nature* **383**, 538-542 (1996).
61. J. Chee *et al.*, Effector-memory T cells develop in islets and report islet pathology in type 1 diabetes. *J Immunol* **192**, 572-580 (2014).
62. Y. Li *et al.*, Stem-like T cells are associated with the pathogenesis of ulcerative colitis in humans. *Nat Immunol* **25**, 1231-1244 (2024).
63. E. P. Hughes, A. R. Syage, D. Tantin, Durable CD4+ immunity: cherchez la stem. *Trends Imm* **45**, 158-166 (2024).
64. J. M. Polo *et al.*, Specific peptide interference reveals BCL6 transcriptional and oncogenic mechanisms in B-cell lymphoma cells. *Nat Med* **10**, 1329-1335 (2004).
65. N. J. Caron, S. P. Quenneville, J. P. Tremblay, Endosome disruption enhances the functional nuclear delivery of Tat-fusion proteins. *Biochem Biophys Res Commun* **319**, 12-20 (2004).
66. S. Krautwald, E. Ziegler, K. Tiede, R. Pust, U. Kunzendorf, Transduction of the TAT-FLIP fusion protein results in transient resistance to Fas-induced apoptosis in vivo. *J Biol Chem* **279**, 44005-44011 (2004).

915 67. H. M. Wright *et al.*, A synthetic antagonist for the peroxisome proliferator-activated receptor
916 gamma inhibits adipocyte differentiation. *J Biol Chem* **275**, 1873-1877 (2000).
917 68. L. T. Vassilev *et al.*, In vivo activation of the p53 pathway by small-molecule antagonists of
918 MDM2. *Science* **303**, 844-848 (2004).
919 69. L. C. Cerchietti *et al.*, A peptomimetic inhibitor of BCL6 with potent antilymphoma effects in
920 vitro and in vivo. *Blood* **113**, 3397-3405 (2009).
921 70. D. R. Green, A BH3 Mimetic for Killing Cancer Cells. *Cell* **165**, 1560 (2016).
922 71. M. Skwarczynska, C. Ottmann, Protein-protein interactions as drug targets. *Future Med Chem*
923 **7**, 2195-2219 (2015).
924 72. G. Lu *et al.*, The myeloma drug lenalidomide promotes the cereblon-dependent destruction of
925 Ikaros proteins. *Science* **343**, 305-309 (2014).
926 73. E. S. Fischer *et al.*, Structure of the DDB1-CRBN E3 ubiquitin ligase in complex with
927 thalidomide. *Nature* **512**, 49-53 (2014).
928 74. W. Fiskus *et al.*, Superior efficacy of co-targeting GFI1/KDM1A and BRD4 against AML and
929 post-MPN secondary AML cells. *Blood Cancer J* **11**, 98 (2021).
930 75. G. C. Issa *et al.*, The menin inhibitor revumenib in KMT2A-rearranged or NPM1-mutant
931 leukaemia. *Nature* **615**, 920-924 (2023).
932 76. I. Antony-Debré *et al.*, Pharmacological inhibition of the transcription factor PU.1 in leukemia. *J*
933 *Clin Invest* **127**, 4297-4313 (2017).
934 77. S. J. Taylor *et al.*, Pharmacological restriction of genomic binding sites redirects PU.1 pioneer
935 transcription factor activity. *Nat Genet* **56**, 2213-2227 (2024).
936 78. S. A. Gibson, W. Yang, Z. Yan, H. Qin, E. N. Benveniste, CK2 Controls Th17 and Regulatory T
937 Cell Differentiation Through Inhibition of FoxO1. *J Immunol* **201**, 383-392 (2018).
938 79. F. Wang *et al.*, Tight regulation of FOXO1 is essential for maintenance of B-cell precursor
939 acute lymphoblastic leukemia. *Blood* **131**, 2929-2942 (2018).
940 80. Z. Klase *et al.*, Activation of HIV-1 from latent infection via synergy of RUNX1 inhibitor Ro5-
941 3335 and SAHA. *PLoS Pathog* **10**, e1003997 (2014).
942 81. J. Zhu, M. Singh, G. Selivanova, S. Peuget, Pifithrin-α alters p53 post-translational
943 modifications pattern and differentially inhibits p53 target genes. *Sci Rep* **10**, 1049 (2020).
944 82. N. B. Struntz *et al.*, Stabilization of the Max Homodimer with a Small Molecule Attenuates Myc-
945 Driven Transcription. *Cell Chem Biol* **26**, 711-723.e714 (2019).
946 83. H. Frangoul *et al.*, CRISPR-Cas9 Gene Editing for Sickle Cell Disease and β-Thalassemia. *N*
947 *Engl J Med* **384**, 252-260 (2021).
948 84. E. Jonasch *et al.*, Belzutifan for Renal Cell Carcinoma in von Hippel-Lindau Disease. *N Engl J*
949 *Med* **385**, 2036-2046 (2021).
950 85. J. H. Bushweller, Targeting transcription factors in cancer - from undruggable to reality. *Nat*
951 *Rev Cancer* **19**, 611-624 (2019).
952 86. M. Bekes, D. R. Langley, C. M. Crews, PROTAC targeted protein degraders: the past is
953 prologue. *Nat Rev Drug Discov* **21**, 181-200 (2022).
954 87. J. Maddox *et al.*, Transcription Factor Oct1 Is a Somatic and Cancer Stem Cell Determinant.
955 *PLoS Genet* **8**, e1003048 (2012).
956 88. K. Vázquez-Arreguín *et al.*, Oct1/Pou2f1 is selectively required for colon regeneration and
957 regulates colon malignancy. *PLoS Genet* **15**, e1007687 (2019).
958 89. W. W. Tang *et al.*, A microRNA-regulated transcriptional state defines intratumoral CD8(+) T
959 cells that respond to immunotherapy. *Cell Rep* **44**, 115301 (2025).
960 90. Y. Jing *et al.*, Increased TCR signaling in regulatory T cells is disengaged from TCR affinity.
961 *bioRxiv*, (2023).
962 91. Y. Liu *et al.*, Designed compounds for recognition of 10 base pairs of DNA with two at binding
963 sites. *J Am Chem Soc* **134**, 5290-5299 (2012).
964 92. D. Tantin, M. Gemberling, C. Callister, W. Fairbrother, High-throughput Biochemical Analysis of
965 in-vivo Location Data Reveals Novel Distinct Classes of POU5F1(Oct4)/DNA complexes.
966 *Genome Res* **18**, 631-639. (2008).

967 93. V. E. Wang, T. Schmidt, J. Chen, P. A. Sharp, D. Tantin, Embryonic Lethality, Decreased
968 Erythopoiesis, and Defective Octamer-Dependent Promoter Activation in Oct-1-Deficient Mice.
969 *Mol Cell Biol* **24**, 1022-1032. (2004).
970 94. A. O. Magnusson *et al.*, nanoDSF as screening tool for enzyme libraries and biotechnology
971 development. *FEBS J* **286**, 184-204 (2019).

972

Du et al. Figure 1

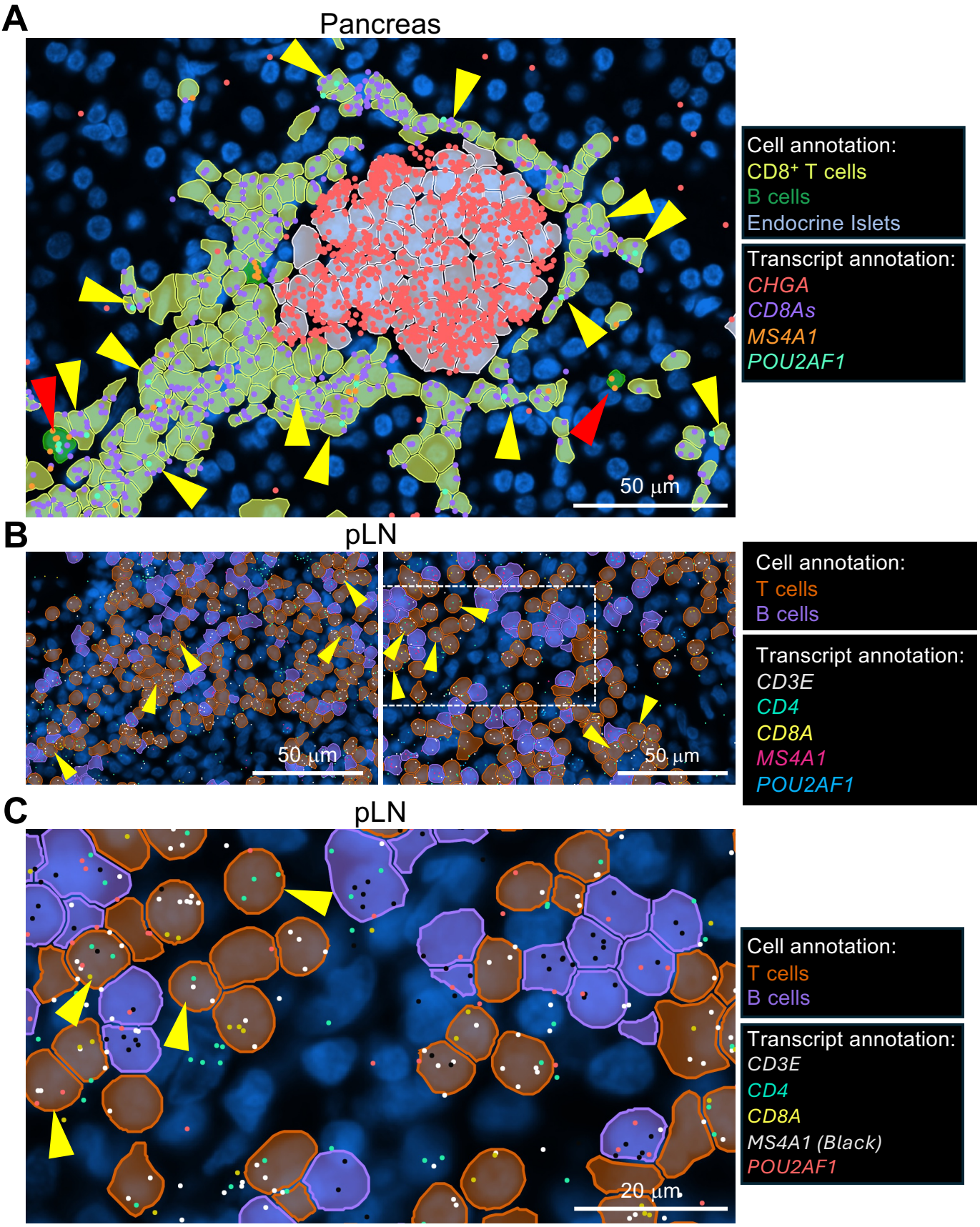

Du et al. Figure 2

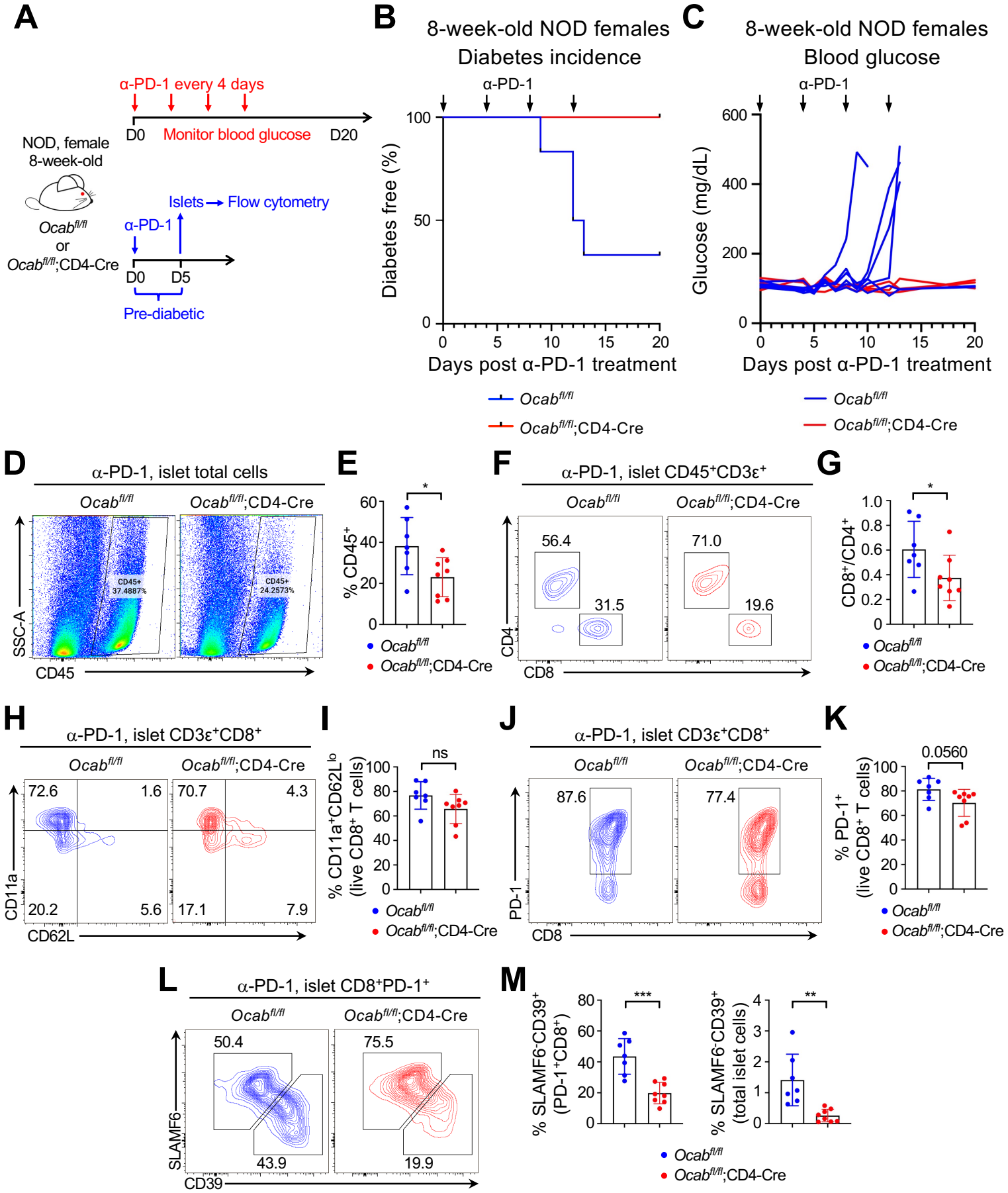

Du et al. Figure 3

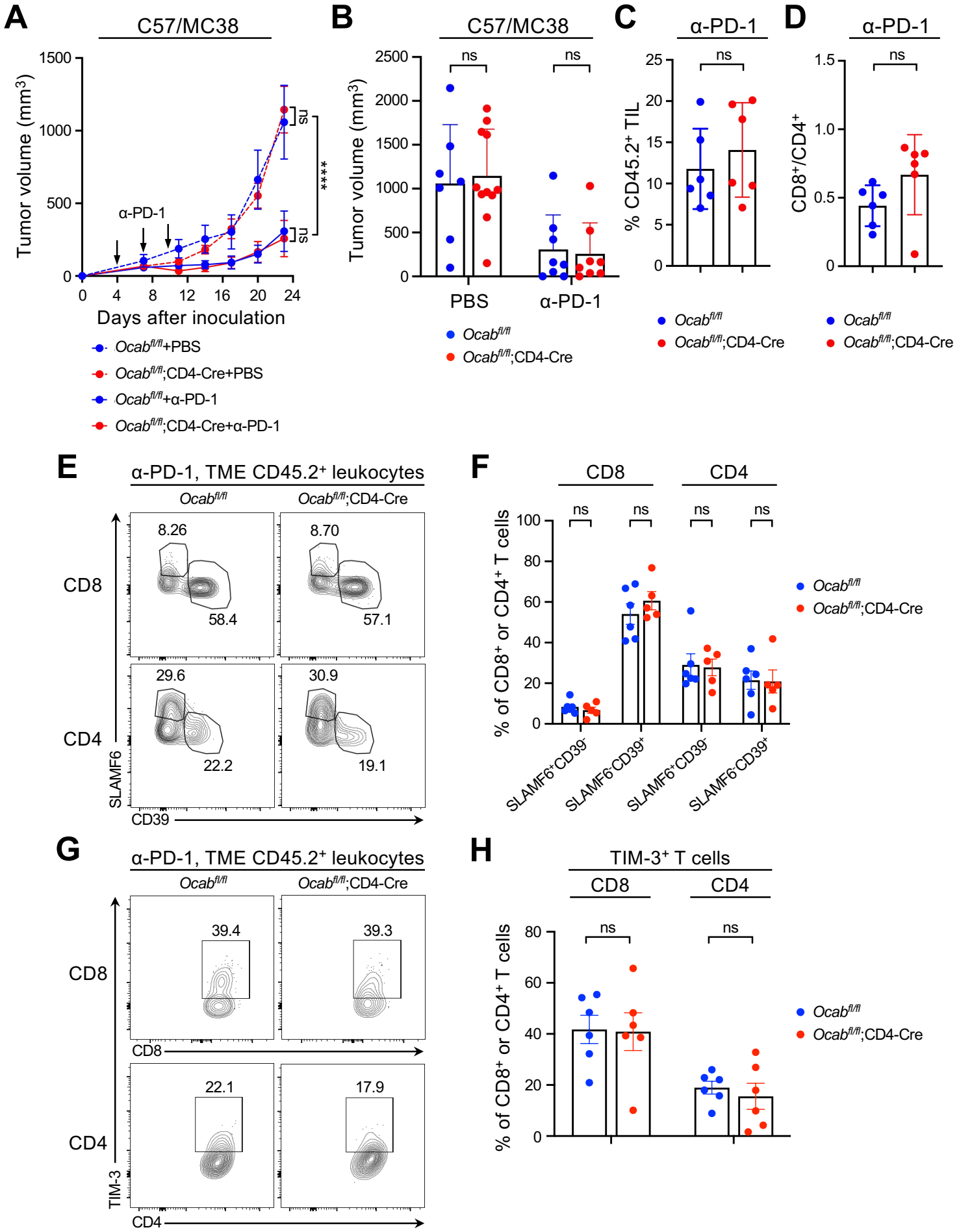

Du et al. Figure 4

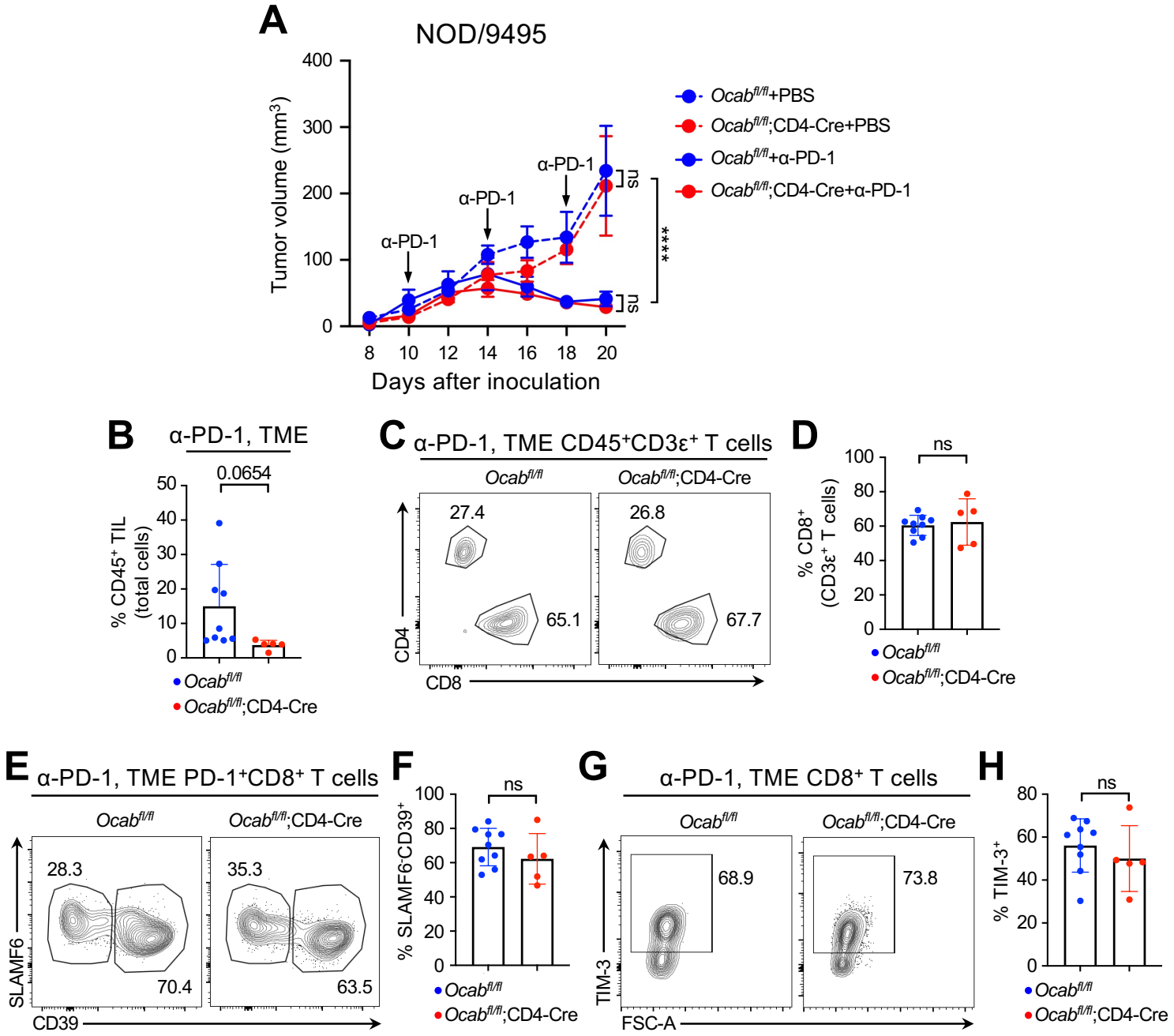

Du et al. Figure 5

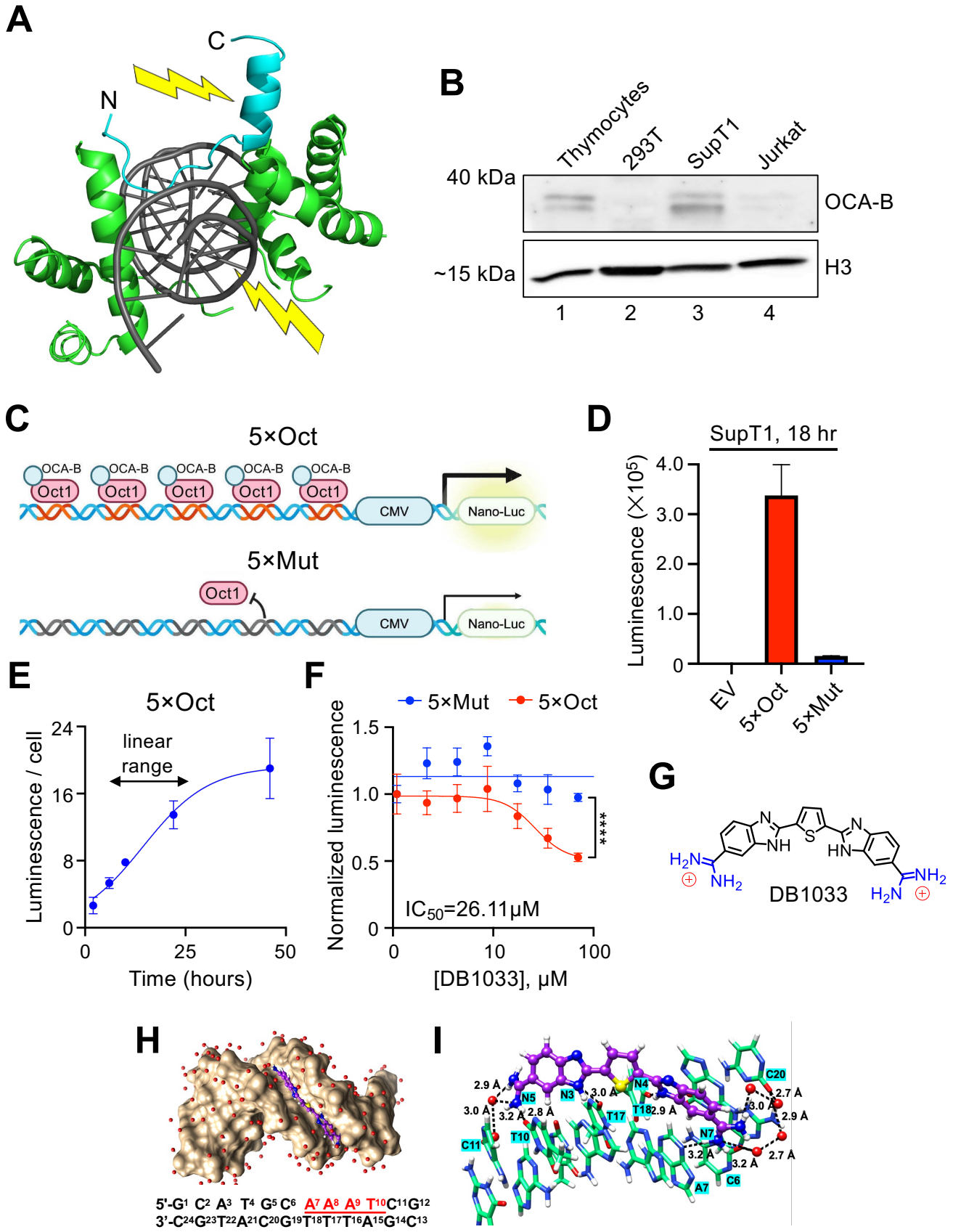

Du et al. Figure 6

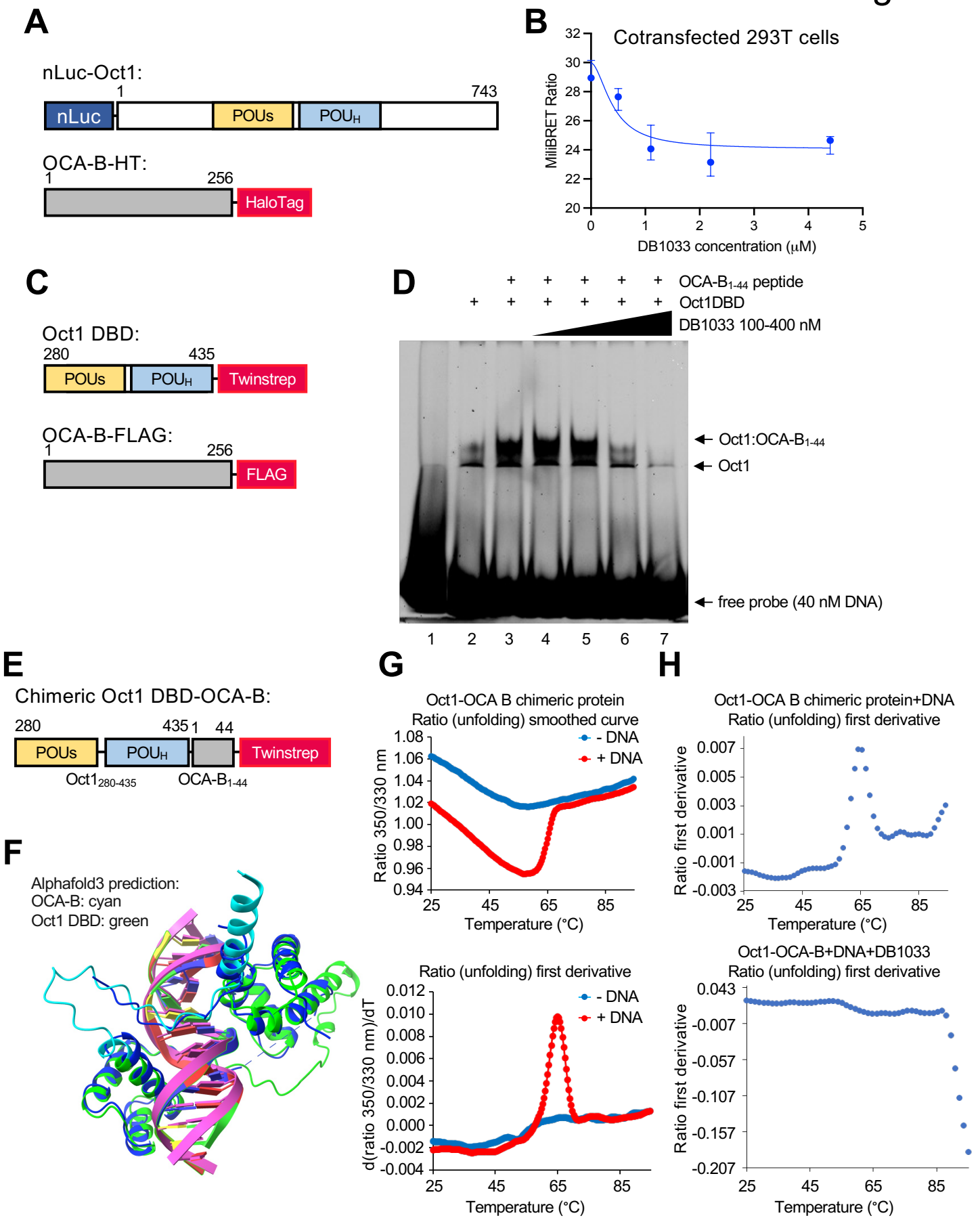
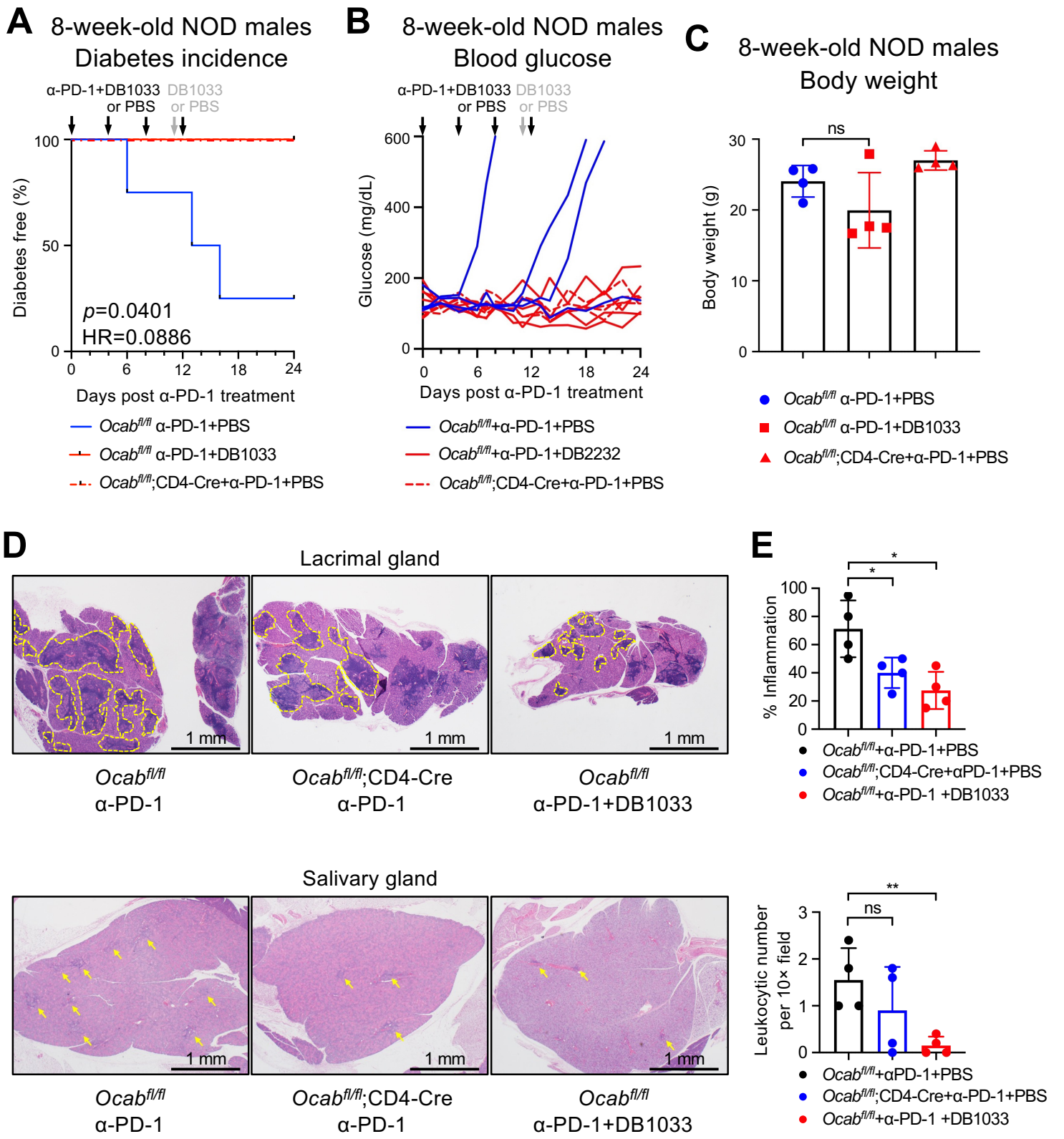
Du et al. Figure 7